The Structure and Nonlinear Evolution of Synoptic Scale Cyclones: Life Cycle Simulations with a Cloud-Scale Model

S. M. POLAVARAPU* AND W. R. PELTIER

University of Toronto, Department of Physics, Toronto, Ontario Canada

(Manuscript received 2 March 1990, in final form 22 May 1990)

ABSTRACT

High resolution simulations of idealized baroclinic wave life cycles on both the f-plane and the β-plane are performed. The anelastic, nonhydrostatic equations are employed in these analyses and motions are assumed dry adiabatic and inviscid, apart from a weak horizontal diffusion. Cyclogenesis is documented in considerable detail and features the formation of an occlusion with spiraling temperature contours that cuts off completely from the main warm air mass late in the life cycle in all cases. Thereafter, the occlusion develops independently of the remaining warm–cold frontal cusp and decays by becoming zonally elongated. Later redevelopment involving reorganization of the occlusion into the more nearly circular shape that obtains at the time of cut-off can reoccur on the f-plane leading to an oscillatory life cycle.

Features of the simulated synoptic scale vortices that are in common with observed cyclones are the comma-shaped vertical velocity pattern, the spiraling temperature and vorticity patterns at the surface, and mesoscale bands of rising air within the occlusion and along the comma tail. The similarity of our results with a variety of observations suggests the potential for dry dynamics alone to explain many of the mesoscale features of actual cyclogenesis events. Many such features are, therefore, plausibly understood as being forced by synoptic scale processes. Within the context of primitive equations dynamics the β-effect is shown to enhance the asymmetry between surface frontal intensities and to cause the occlusion to develop farther north than is characteristic on the f-plane.

1. Introduction

The need for an hierarchy of models (numerical, analytical, and laboratory) of varying complexity, not only to understand the process of midlatitude cyclogenesis but also to assist in the development of conceptual models that are in closer accord with observations than is the Polar Front theory (e.g., Bjerknes and Solberg 1923), was stressed by Hoskins (1983) and reiterated more recently by Keyser (1989). With the advent of very high speed supercomputers, it has become possible to explicitly model the complete nonlinear evolution of baroclinic waves in three spatial dimensions. Using recently developed numerical techniques, an hierarchy of numerical models of varying complexity has been designed to study nonlinear baroclinic wave evolution under both idealized and more realistic conditions. The analyses to which we shall specifically refer are those whose primary intent has been to improve understanding of the processes through which idealized baroclinic waves develop based upon application of such three-dimensional numerical simulation techniques.

The first in this modern series that we see as important was the study by Mudrick (1974), which compared the evolution of a baroclinically unstable wave under the assumption of hydrostatic, Boussinesq primitive equations dynamics with one evolving quasi-geostrophically. Both systems were formulated on a β-plane and motions were assumed to be dry and adiabatic. As in the Polar Front theory of Bjerknes and others, warm and cold fronts were shown to form, but not with the typical cusp-like organization suggested by this conceptual model. In the simulation based upon the quasi-geostrophic equations, the surface fronts that formed were symmetric in position and intensity. However, the primitive equations permitted asymmetries between these fronts to develop. In fact, a sharp surface warm front formed at the leading edge of the warm air and this front was the most intense of the three identified. Mudrick pointed to the importance of horizontal advection by the divergent component of the wind for the formation of the more realistic fronts that appeared in the non quasi-geostrophic simulation.

The nonlinear semigeostrophic equations on an f-plane were employed by Hoskins (1976) to study the development of a doubly periodic Eady wave. The ageostrophic advection retained in the semigeostrophic equations was able to produce the asymmetric cold and warm front intensities seen with the primitive equations. In a continuation of this study, Hoskins and West (1979) considered the baroclinic instability of an upper level westerly jet flow. As in the analyses of

* Current address, Aerospace Meteorology Division, Atmospheric Environment Service, Downsview, Ontario, Canada, 53H-5T4.

Corresponding author address: Dr. W. R. Peltier, Department of Physics, University of Toronto, Toronto, Ontario, M5S 1A7, Canada.

© 1990 American Meteorological Society

Mudrick (1974), a sharp warm front formed first at the leading edge of warm air. Heckley and Hoskins (1982) included a stratosphere and some tropopause folding was then observed to occur.

The nonlinear simulations of Simmons and Hoskins (1978, 1980), based upon the use of the hydrostatic primitive equations on a sphere, identified a well-defined life cycle consisting of baroclinic growth and barotropic decay. However, in considering barotropic influences on the evolution of baroclinic waves in the latter study, a life cycle with two peaks in eddy kinetic energy was found for one mean flow. The effect of baroclinic disturbances on the mean flow was shown to consist of the reduction of baroclinicity in central latitudes and the creation of baroclinic regions to the north and south. The nonlinear waves were shown to have similar life cycles to those simulated by Hoskins and West (1979) on an f-plane. No occlusion was observed to occur in this or any of the aforementioned studies, although Hoskins (1983) described a single simulation in which the occlusion process appeared to have begun but did not go to completion.

Golding (1984) demonstrated that for idealized nonlinear baroclinic waves the inclusion of moisture intensifies and accelerates cyclogenesis. Convective activity was shown to occur along the surface cold front and slow upgliding motions were found along the warm front. Here too, although occlusion of the cyclone began, it did not continue to completion.

One of the most advanced numerical descriptions of the occlusion process that is available in the literature is that recently obtained by Takayabu (1986) using the hydrostatic primitive equations on a β-plane. Instead of occurring as the cold front overtakes the warm front however, as the Polar Front theory hypothesizes, warm air at the leading warm front was found to turn cyclonically at the surface, spilling into the cold air. Suggestions of the beginnings of similar occlusion processes were seen in all of the simulations cited above and more completely in the very recent f-plane analysis of Keyser et al. (1989). The work of Keyser et al. (1989) captured many of the features of cyclogenesis that were first shown in publications preliminary to the present analyses (Peltier et al. 1988, 1990).

Another disagreement between the Polar Front theory and the idealized baroclinic-wave life cycle simulations that have been performed to date concerns the existence of a cusp shaped warm and cold front pattern at the surface. Such a cusp was not seen in any of the pre-1988 simulations except very late in the evolution after occlusion had begun in the simulation of Takayabu (1986). Furthermore, the cold front was not found to be the first frontal feature to form. Rather, a warm front at the leading edge of northward moving warm air formed first and a strong cold front appeared only late in the simulations employing nongeostrophic dynamics.

Clearly, the polar-front theory of cyclogenesis requires some modification to account for the results of these theoretical numerical simulations and the more recent conceptual models based on composite observations such as the conveyor belt model (Carlson 1980), the split front model (Browning and Monk 1982), the dry intrusion model (Young et al. 1987) and the very recent observations of Shapiro (1989) and Shapiro and Keyser (1990). However, there remain some aspects of idealized cyclogenesis that must first be clarified, such as the designation and position of the surface fronts. There is already much agreement among the above simulations regarding the formation of a "leading" warm front before an intense cold front appears. This is seen most clearly in Takayabu's study and he attempts to compare his findings with the polar-front theory. It has not yet been suggested that it may be more appropriate to regard this first forming front as the warm front, at least until occlusion has occurred, by which time the standard warm front has intensified. More importantly, the process of occlusion has not been adequately examined in any of the previous studies of idealized baroclinic wave evolution cited above. This will, therefore, be one focus of the present paper.

In what follows, we shall present a number of nonlinear simulations of baroclinic-wave life cycles in an attempt to clarify some of the remaining issues. In particular, we are interested in extending the description of dry, adiabatic cyclogenesis to include the occlusion process and also in understanding the asymmetry of surface cold and warm fronts. We extend the range of complexity of these models by explicitly contrasting cyclogenesis on the f-plane with that on the β-plane. As we shall see, the beta effect appears to be responsible for a number of features that allow the model simulations to reproduce many of the detailed characteristics of observed cyclones. The mesoscale structure that develops within the model cyclones, in particular, is very suggestive of a number of dynamical features commonly found within synoptic scale systems, as we shall see.

We shall first describe the numerical model and the parameter settings employed, the initial fields, and the numerical formulations developed for energy budget analyses. We shall then present the simulated life cycles in terms of surface fields and vertical cross sections, mean fields and surface frontogenesis. The importance of nonhydrostatic motions in these dry, inviscid simulations will be specifically assessed. We conclude with a brief summary of our main results.

2. The numerical model

In order to simulate the nonlinear evolution of baroclinic waves we have chosen to employ the anelastic, nonhydrostatic model of Clark (1977). This model, initially designed for problems of small horizontal scale (e.g., mountain waves: Peltier and Clark 1979; Kelvin–Helmholtz waves: Peltier et al. 1978; cumulus clouds: Clark 1979) has the advantage of including nonhy-

drostatic effects and is, therefore, capable of accurately describing the deep vertical motions of small horizontal scale that may accompany the cascade of energy in cyclogenesis. Such motions, normally considered unimportant in this process, are expected to be necessary for accurate simulation of the evolution of mesoscale structures within cyclones and perhaps also for the representation of subsynoptic cyclogenesis. The other principal advantage of this model is its inclusion of cloud physical parameterizations that will facilitate the explicit incorporation of moist processes in future studies of baroclinic wave evolution. Finally, by attempting to employ a cloud scale model for the purpose of simulating the nonlinear life cycle of a baroclinic wave, we will be able to test the hypothesis that planetary or synoptic scale phenomena might be adequately simulated using models designed for smaller scale processes.

Since the numerical model has been well documented previously in the literature (e.g., Clark 1977, 1979), we will point only to a few of its most important characteristics here. A leap-frog scheme in time is employed with an Euler-backward step performed every 20 time steps to prevent splitting of the computational and physical modes. The model allows for the incorporation of a Robert–Asselin time filter (Asselin 1972) but it was found unnecessary for our simulations so it was not employed. The Smolarkiewicz (1983, 1986) advection scheme, which minimizes false diffusion in the advection of scalar fields while maintaining positive values for positive definite scalars, was utilized for the potential temperature field.

We employ horizontal diffusion in the form of a highly scale selective ∇^6 horizontal smoothing operator. This filter was found to preserve the coherence of the fields in the later stages of evolution of the wave while minimizing energy dissipation (as will be apparent in the energy balance analyses presented below). Hence, the runs are nearly inviscid in that energy is almost in balance throughout the simulations and will, henceforth, be referred to as inviscid.

No surface friction or Ekman layer has been included in the analyses that we shall present. In addition, the model is dry and motions are adiabatic. Diabatic and frictional processes were omitted in these simulations in order to develop a database that we will later be able to employ for purposes of comparison with calculations that will include these and other effects. Since we are concerned here with idealized baroclinic wave evolution it is necessary to first establish the nature of cyclogenesis in dry, inviscid dynamics before proceeding to include additional realistic processes.

The model has rigid horizontal surfaces that bound the fluid from both above and below. We require that

$$w = 0 \quad \text{on} \quad z = 0, H$$

where H is the height of the model. Since the initial disturbance will be isolated by the applied baroclinicity in the center of the domain, we may impose rigid vertical walls at the meridional boundaries; i.e.,

$$v = 0 \quad \text{at} \quad y = 0, L_y$$

where L_y defines the meridional extent of the numerical domain. In the zonal direction, the flow will be assumed periodic. We, therefore, choose boundary conditions in x such that

$$\psi(x + L_x) = \psi(x)$$

where the length L_x is chosen to be exactly one wavelength of the fastest growing mode of linear stability theory (see below).

3. The initial fields

The fields employed to inialize each of our three-dimensional time dependent simulations consist of two components: a mean state and a wave. A linear anelastic stability analysis is performed on the mean state (as described in Moore and Peltier 1987, 1990, except that the calculations have been extended to incorporate anelasticity and the β-effect) to determine the structure and wavelength of the fastest growing mode on the long-wave (Eady) branch of baroclinically unstable waves. This wavelength determines the zonal extent of the model. The amplitude of the wave was chosen to be small in order to reduce the shock of start-up. The wave fields that are delivered by the linear stability analysis are obtained on a grid that differs from the grid of the nonlinear model, and interpolation was necessary. Some difficulties with the start-up phase of the integrations are, therefore, inevitable. The two-dimensional mean state was adjusted to be in exact hydrostatic and geostrophic balance with respect to the model equations using an iterative procedure described in Polavarapu (1989, hereafter referred to as I). Hence, the initial mean state is steady to machine precision on the model grid.

All mean states that we have employed in this work consist of broad baroclinic zones of two general types. The first is characterized by two zonal jets blowing in opposing directions (a westerly jet with maximum velocity on the upper lid of the model and an easterly jet with maximum velocity at the earth's surface). The second type consists of a single westerly jet centered on the upper lid. The former class of mean states (denoted HBF) was created through the process of semi-geostrophic frontogenesis forced by a hyperbolic deformation field on an f-plane as described by Hoskins and Bretherton (1971, 1972). A corresponding minimally perturbed mean state in thermal wind balance on the β-plane was found through the process described in I and is denoted HBB. The second type of mean state, which is more analogous to the zonally and temporally averaged flow at midlatitudes, is prescribed as in I and is similar to that employed by Hoskins and

West (1979). This mean state and its counterpart on the β-plane are denoted HWF and HWB, respectively.

All four mean states are shown in Fig. 1. Note that theta refers to a potential temperature deviation from a constant background value. All domains are 5500 km in meridional extent and 8 km high and have rigid upper and lower horizontal boundaries. The parameters describing each model are listed in Table 1. Other parameters are as follows:

$$f_0 = 10^{-4}\ \mathrm{s}^{-1} \quad \beta = 1.667 \times 10^{-11}\ \mathrm{m}^{-1}$$

$$P_0 = 1000\ \mathrm{mb}$$

$$g = 9.81\ \mathrm{m\ s}^{-2} \quad c_p = 1004\ \mathrm{J\ kg}^{-1}\ \mathrm{K}^{-1}$$

$$c_v = 717\ \mathrm{J\ kg}^{-1}\ \mathrm{K}^{-1}$$

Visual comparison of the f-plane and β-plane forms for the two distinctly different mean states demonstrates that the introduction of the β-effect has only a slight impact on the zonal wind field. The fact that these initial mean states differ so slightly is important because differences in the nonlinear evolution of the baroclinically unstable waves between f-plane and β-plane simulations will, therefore, be attributable to the influence of β on the wave rather than to differences in the mean states.

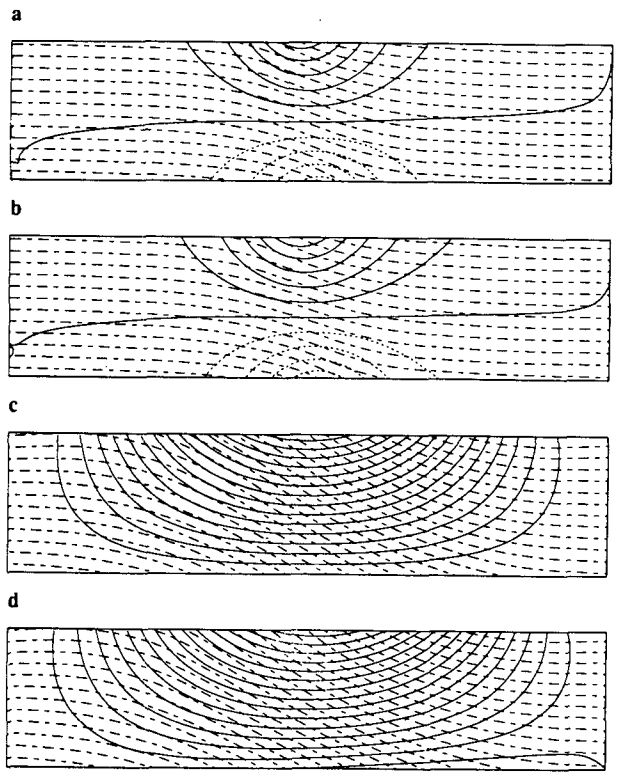

FIG. 1. The four mean states employed. Potential temperature deviation from a background constant value (dash-dot) and along front or zonal velocity (solid; negative values dashed) fields are given. Contour intervals are 2 K and 2 m s^{-1}: (a) HBF, (b) HBB, (c) HWF, (d) HWB.

The structure of the wave fields determined from linear stability analyses are indicated in Fig. 2 for the HWF case. The amplitude shown is 1 K in the temperature field and all fields are shown at the surface. The correlation of warm air flowing northward and upward is evident. There is a slight NW–SE tilt to the fields. There are differences in the structure of the linear waves for the four mean states. There is a pronounced NW–SE tilt to the fields north of the perturbation maximum and a less steep NE–SW tilt south of the maximum for HWB. For HWF only a slight reverse tilt exists in the south. Because the baroclinic zone is wider in the HW mean states (Fig. 1) the perturbations are broader in the meridional direction. For the same amplitude, the vertical velocity perturbation is also smaller for the HB mean states and slightly smaller on the β-plane than on the f-plane for both mean states.

4. Energetics of the model

In order to understand the physical processes occurring in the model it is useful to define the quantities that appear in a detailed energy budget. Because the simulations under consideration employ a mean state that is initially uniform in the x or zonal direction, it is convenient to consider energy through the zonally averaged and departures from zonally averaged parts. Let

$$u = \bar{u} + u'$$

where

$$\bar{u} = \frac{1}{L_x}\int_0^{L_x} u\,dx$$

for a domain of zonal length L_x. It will prove convenient for this discussion to define the following integral operators, for some arbitrary function $\psi(x, y, z, t)$, as

$$\{\psi\} = \frac{1}{L_x}\int_0^{L_x} \psi\,dx \tag{1}$$

$$\langle\psi\rangle = \frac{1}{L_y}\int_0^{L_y}\frac{1}{H}\int_0^{H} \psi\,dz\,dy. \tag{2}$$

Since the model employs periodic boundary conditions in the x or zonal direction, $\{\psi'\} = 0$ for all perturbation quantities. Then the total kinetic energy is given by

$$K = \bar{K} + K'$$

where

$$\bar{K} = \frac{1}{2}\overline{\overline{\rho}^{x}\,\overline{u}^{x\,2}} \tag{3}$$

$$K' = \frac{1}{2}\left\{\overline{\overline{\rho}^{x}\,u'^2}^{x} + \overline{\overline{\rho}^{y}\,v^2}^{y} + \overline{\overline{\rho}^{z}\,w^2}^{z}\right\}, \tag{4}$$

and where the averaging operations are represented by

TABLE 1. The model parameters for the various simulations. Wavenumbers have been nondimensionalized by NH/f = 800 km. All domains are 5500 km × 8 km in the meridional and vertical directions. The channel lengths are $2\pi NH/(fb)$ km for nondimensional wavenumber b.

Name	Number of points (x, y, z)	Wave number	Grid size (km)	Time step (sec)	Wave amplitude (K)
HBF	63 111 17	1.62	50 50 .5	180	1
HBB	63 111 17	1.80	45 50 .5	180	1
HWF	63 111 17	1.60	51 50 .5	180	.5
HWB	63 111 17	1.60	51 50 .5	180	.5
HBBH	93 199 17	1.80	30 28 .5	180	1
HWBH	93 199 17	1.60	34 28 .5	180	.5

Shuman operators (Clark 1977; Shuman 1962). These definitions, (3) and (4), are useful because in the early stages of wave growth we can simply relate $\bar{K}$ to the mean flow kinetic energy and K' to the wave kinetic energy.

The energy balance can be summarized as follows:

$$\delta_t\langle\{\bar{K}\}\rangle = C(K', \bar{K}) \tag{5}$$

$$\delta_t\langle\{K'\}\rangle = -C(K', \bar{K}) - C(K', P) \tag{6}$$

$$\delta_t\langle\{P\}\rangle = C(K', P) \tag{7}$$

where

$$P = -\bar{\rho}^z g z \bar{\theta}^{*tz}, \tag{8}$$

$$C(K', P) = -\langle\{\overline{\bar{\rho}^z g \tilde{w} \tilde{\theta}^{*z}}^z\}\rangle, \tag{9}$$

$$C(K', \bar{K}) = \langle\{\overline{\bar{\rho}^y v \overline{\tilde{u}'\tilde{u}}^{xy}}^x \delta_y \tilde{u}\}\rangle + \langle\{\overline{\bar{\rho}^z w \overline{\tilde{u}'\tilde{u}}^{xz}}^x \delta_z \tilde{u}\}\rangle. \tag{10}$$

Here $C(K', P)$ represents the conversion of potential energy to eddy kinetic energy (kinetic energy associated with departures from a zonally averaged flow) through the transport of warm fluid upward and cold fluid downward. Thus, this term has been denoted VHF (vertical heat flux). We associate baroclinic processes with large positive VHF though more precisely it refers to both horizontal and vertical transfers of heat. Past studies (e.g., Simmons and Hoskins 1978) have demonstrated that the two components are well correlated throughout the life cycle of the baroclinic wave. Furthermore, the calculation of Eliassen–Palm fluxes also verifies this for our simulations. We shall refer to K' as EKE and $\bar{K}$ as ZKE hereafter. $C(K', \bar{K})$ consists of two terms: horizontal and vertical Reynolds stresses that represent the transport of zonal momentum northward and upward. The quasi-geostrophic equations of motion omit the vertical stress term (VRS).

The sum of (5)–(7) implies conservation of total energy throughout the simulations due to the absence of dissipative processes in our dynamical system. For simulations with no diffusion, energy balance was well preserved. Hence, the energy lost through the horizontal smoothing process can be estimated as the departure from exact energy balance.

5. Results

The following discussion is based on the analysis of six simulations. However, we are mainly concerned with four of these: HBF, HBB, HWF and HWB (see

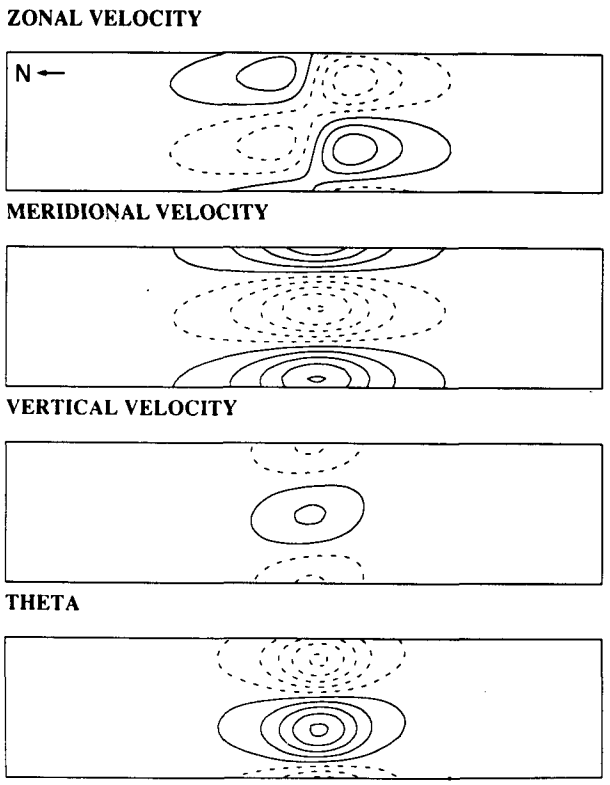

FIG. 2. The structure of the perturbation at the surface for an amplitude of 1 K for the HWB mean state. North is in the $-x$ direction and east is in the $+y$ direction. Negative values are dashed. Contour intervals are 0.4 m s^{-1}, 0.4 m s^{-1}, 0.04 cm s^{-1} and 0.2 K. Solid contours represent eastward, southward, or upward velocities.

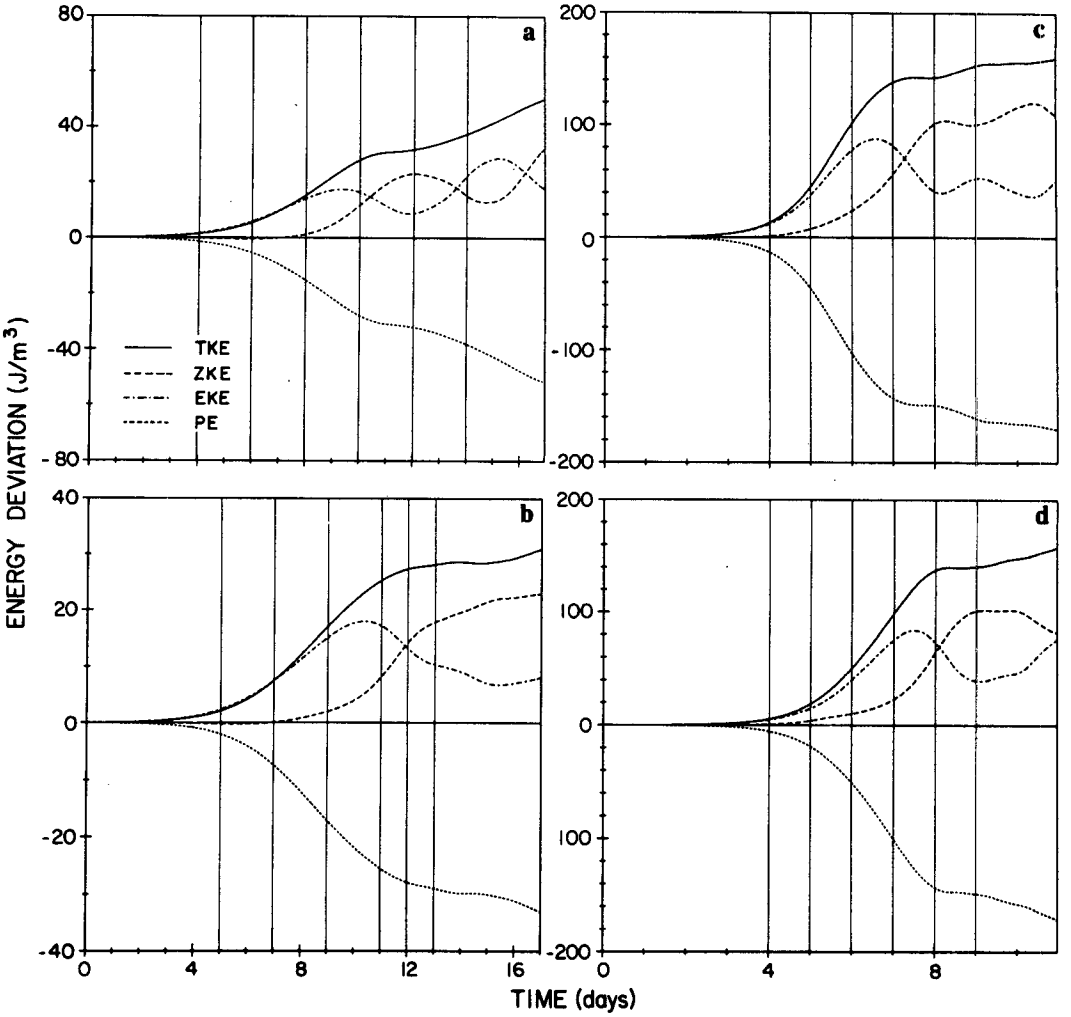

FIG. 3. The energetics of the four simulations: (a) HBF, (b) HBB, (c) HWF, (d) HWB. ZKE + EKE (solid), EKE (dash-dot), ZKE (dashed) and PE (dotted) minus initial values are given. The solid vertical lines indicate the times for which the horizontal cross sections are shown.

Table 1 for parameters associated with these simulations). The resolution of these runs is approximately 50 km in the horizontal and 0.5 km in the vertical. Additional high resolution simulations (HBBH and HWBH) with grid spacing of approximately 30 km in the horizontal were performed for the simulations on the β-plane.

a. Energetics

Figure 3 describes the evolution of the zonally averaged kinetic energy (ZKE, dashed lines), the departure from zonally averaged flow (EKE, dash-dots), the total kinetic energy (TKE = ZKE + EKE, solid lines) and the potential energy (PE, dots) for the four main simulations. The energy at the initial time has been subtracted so that all values are initially zero. In each case the EKE rises rapidly, peaks, then falls at the same rate at which it rose. At the time that the EKE is falling, a pronounced growth in ZKE is occurring. The EKE peak is due to the creation of a cyclonic circulation in conjunction with the development of a closed low pressure anomaly at the surface. The peak is associated with "wave saturation" (e.g., Simons 1972). In the linear stability analyses of I, the mean flow was assumed to be stationary and theory then predicts that the fluctuation grows exponentially in time. However, once nonlinear effects are permitted the mean state becomes more stable with respect to the wave than it was initially and the wave amplitude saturates. Of course Figs. 3a and 3c show that further episodes of wave growth and decay are possible.

The numerical simulations of Simmons and Hoskins (1978) and the atmospheric observations of Randel and Stanford (1985) describe baroclinic-wave life cycles consisting of a single peak of eddy kinetic energy. The

wave grows baroclinically and decays barotropically. In contrast, Fig. 3a describes an oscillation in EKE for the HBF run. The peak in EKE is associated with cyclogenesis on the surface and lid (stronger at the lid due to anelastic effects). The peak in ZKE is associated with the development of a high pressure center at the surface. Subsequent reintensification of the surface low accounts for the second rise in EKE. The period of this oscillation is about 5–6 days for this model in which the baroclinicity is rather weak. For HWF there is a similar oscillation of EKE to that delivered by the HBF simulation but this is of smaller amplitude (Fig. 3c). This oscillation has a period of approximately 2 days. Recent simulations of two-dimensional Eady waves (Eady 1949) have also been shown to be characterized by oscillations in EKE (Nakamura and Held 1989).

To determine whether the oscillation on the f-plane was due to the presence of vertical walls at the north and south boundaries, we increased the meridional extent by 20%. If the oscillation was due to a resonance such an increase would drastically alter the energetics. In fact, the energetics were not visibly different in these two HBF cases, indicating that internal dynamics is responsible for the oscillation. Nevertheless, as we shall see later, the boundaries can influence the dynamics in other cases and when this occurs the simulation is aborted.

In contrast, for the HBB run on the β-plane (Fig. 3b), the EKE exhibits only one primary peak. The slight rise of EKE at day 17 is absent in a higher resolution simulation (HBBH). There also appears to be an oscillation for the HWB case on the β-plane (Fig. 3d), although a higher resolution simulation of the same flow (HWBH) did not display any regular oscillation. The rapid rise in EKE between days 10 and 11 is not observed. It is, therefore, tempting to suggest that there is a simple relation between the EKE oscillation and the β-effect. However, Simmons and Hoskins (1980, their Fig. 6) describe one case in which a second EKE peak did develop. This simulation was also for a mean state that consisted of a single upper level westerly jet; but their calculations were on the sphere rather than the β-plane. MacVean (1985) also observed a double peak in EKE for his simulation on a sphere. In addition, Wood (1988) observed oscillations in EKE in his model of an oceanic density front that was formulated in Cartesian geometry on a β-plane. The question then arises as to whether the occurrence of these oscillations is dependent only on the mean state or whether the dynamics of the f-plane are fundamentally different from those of the β-plane. In order to address this question it is necessary to first discover the nature and cause of the oscillations. This goal is pursued in a forthcoming paper.

For HWF and HWB the energy levels of the first EKE peak are similar (slightly smaller on the β-plane) but much larger than those achieved in HBF and HBB. This reflects the enhanced baroclinicity of these mean states as indicated in Fig. 1. The initial horizontal temperature difference across the domain was approximately 10°C for the HB cases but 30°C for the HW cases. The latter value is more representative of the average meridional temperature difference at midlatitudes (e.g., Palmèn and Newton 1969). The increase in energy at the time of wave saturation is greater than this three-fold difference of baroclinicity in the initial state might suggest, due to the nonlinearity of the flow.

It is apparent in Fig. 3 that the energy lost through diffusion is small. At each time step the change in total KE plus PE is balanced to approximately 1%. In the early stages of wave growth, the energy imbalance can be as low as 0.1% but as some energy is lost to diffusion later in the simulations the balance can deteriorate to 10%. The accumulated imbalance over time is what appears in Fig. 3. For the HW mean states the energy lost through horizontal diffusion is more apparent in Fig. 3, particularly near the end of the simulations. Because of the increased intensity of the cyclogenesis, stronger fronts were induced and more energy was diffused to prevent gradients from becoming too large for the fields to be sufficiently resolved.

Not only is cyclogenesis more intense in HWF and HWB but it is also more rapid. The primary cyclogenesis event is over (the time of the first EKE minimum) in 8 days for HWF and 9 days for HWB. Note also that the initial amplitude of the perturbation was smaller for these simulations than for HBF and HBB. The reduced time scale for HWF and HWB is commensurate with observed long wavelength cyclogenesis events (e.g., Emanuel 1986). While the time of the EKE peak in our simulations is dependent upon the initial amplitude of the applied perturbation, the point to be made here is simply that for the parameters chosen for the HWF and HWB runs, the evolution time is similar to that of observed events.

Figure 4 presents the growth rate of the eddy kinetic energy for the four main simulations in which an inertial oscillation is apparent initially but which rapidly decays. This oscillation is forced by an initial incompatibility of the wave fields with the model equations. The amplitude of this oscillation is smaller for HWF and HWB due to the smaller initial perturbations employed. In only 1 case, HBF, does there appear to be a substantial period of linear growth before the rate of growth declines. In HBB the growth rate rises above the linear rate before falling. This is also true for HWB. In HWF beyond the linear regime, the growth rate slightly rises before falling. In all cases, the rate of EKE growth eventually declines, becoming zero in 6–10 days. The growth rate then continues to fall indicating a loss of EKE. The dashed lines in Fig. 4 denote the growth rate predicted by the linear theory developed in I. Comparison is made difficult by the presence of the inertial oscillation and when exponential growth does not persist for a sufficient length of time. On the basis of the nonlinear growth rates calculated as de-

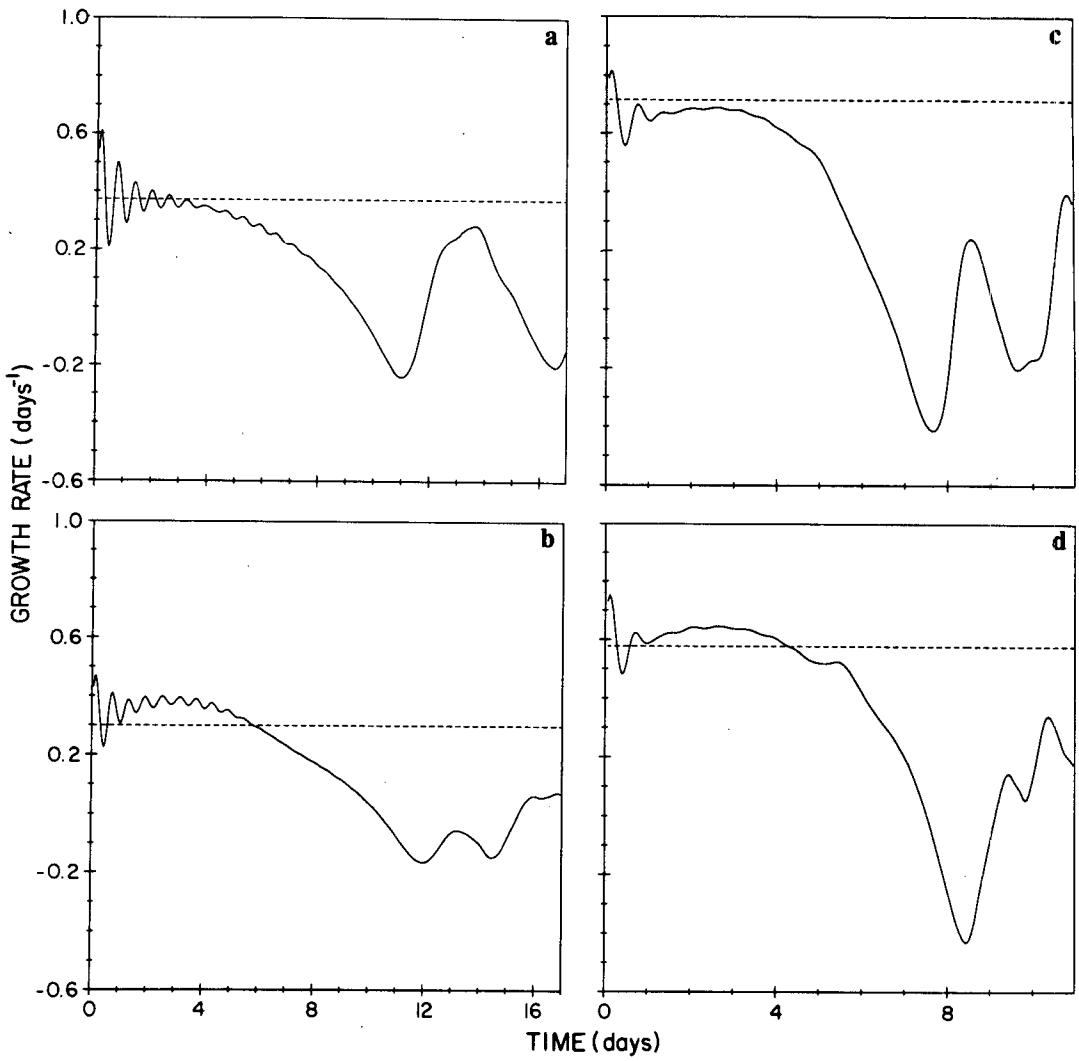

FIG. 4. The growth rate of EKE for (a) HBF, (b) HBB, (c) HWF, (d) HWB. The dashed line indicates the growth rate predicted by linear theory.

scribed above, we roughly estimated a period of linear growth of 1 day on the β-plane, 1.5 days for HWF and 2.5 days for HBF. As we shall see, the presence of β dictates a rapid entry into the nonlinear regime of wave growth (and, implicitly, the increased importance of wave–wave interactions).

Figure 5 presents the temporal evolution of the energy conversion terms for the four main simulations. In all cases, EKE grows through vertical heat flux (baroclinic) terms and decays through horizontal Reynolds stress (barotropic) terms. The time lags between the VHF and HRS peaks are indicated in Table 2. Note that HRS may become positive late in the life cycle of the wave. This means that barotropic conversions of energy are contributing to (rather than depleting) EKE.

The smoothness of the curves in Figs. 3–5 is due to the large number of data points represented. Energies and conversion rates were computed once per hour during the simulations.

b. *Surface cyclogenesis*

Our experiments very much follow in the sequence of numerical cyclogenesis studies, which includes those by Mudrick (1974) and Takayabu (1986). As in these previous analyses we employ Cartesian geometry and the primitive equations but unlike them we have allowed for anelastic and nonhydrostatic effects. In addition, we have continued the trend towards the use of finer resolution in all spatial directions. Less realistically, however, we have not included a stratosphere so that cyclogenesis on the upper lid occurs.

The physical characteristics of a cyclogenesis event are influenced by the mean state in which it occurs.

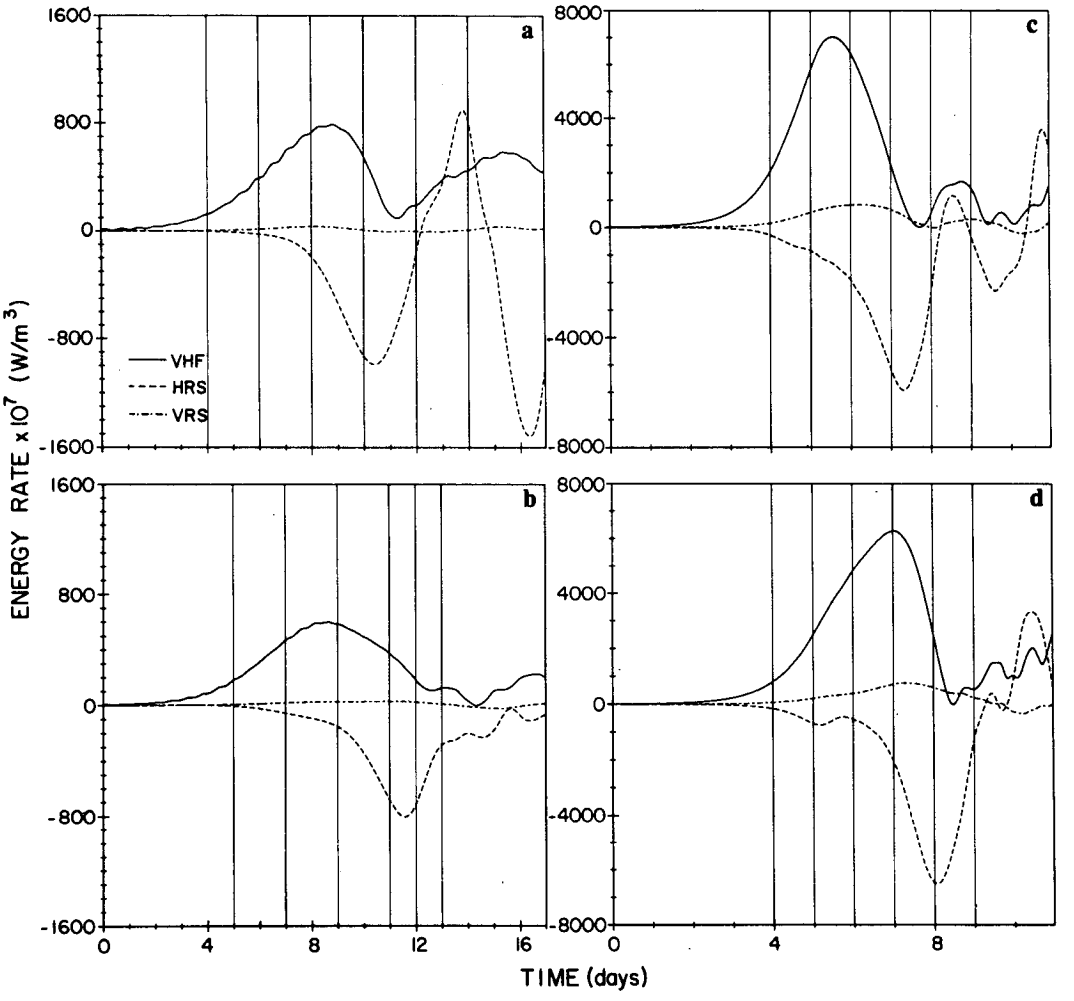

FIG. 5. Energy conversions for (a) HBF, (b) HBB, (c) HWF, (d) HWB. The vertical heat flux (solid), horizontal Reynolds stress (dashed) and vertical Reynolds stress (dash–dot) are indicated.

To illustrate this we will proceed to describe the four main simulations whose characteristics are listed in Table 1 individually and will follow this with a general discussion of the process and energetics of cyclogenesis on the synoptic scale as represented in our model simulations.

1) HBF

Figure 6 depicts the time evolution of the surface potential temperature field for HBF. By day 10, a large occlusion featuring spiraling temperature contours has formed. Such detail, which has not been revealed in

TABLE 2. Some characteristics of the energetics of the nonlinear simulations.

Name	Primary EKE peak		Time lag between HRS, VHS peaks (h)	Primary VHF peak		−HRS/VHF
	Time (h)	Amplitude (J m^{-3})		Time (h)	Amplitude (10^{-5} W m^{-3})	
HBF	224.5	17.5	37	212.5	7.9	0.58
HBB	248.5	17.9	81	196.5	5.9	0.18
HWF	158.5	87.7	41	134.5	70.2	0.19
HWB	180.5	83.7	25	168.5	62.7	0.34
HBBH	248.5	17.9	82	196.5	5.9	0.17
HWBH	180.5	84.3	25	168.5	62.2	0.35

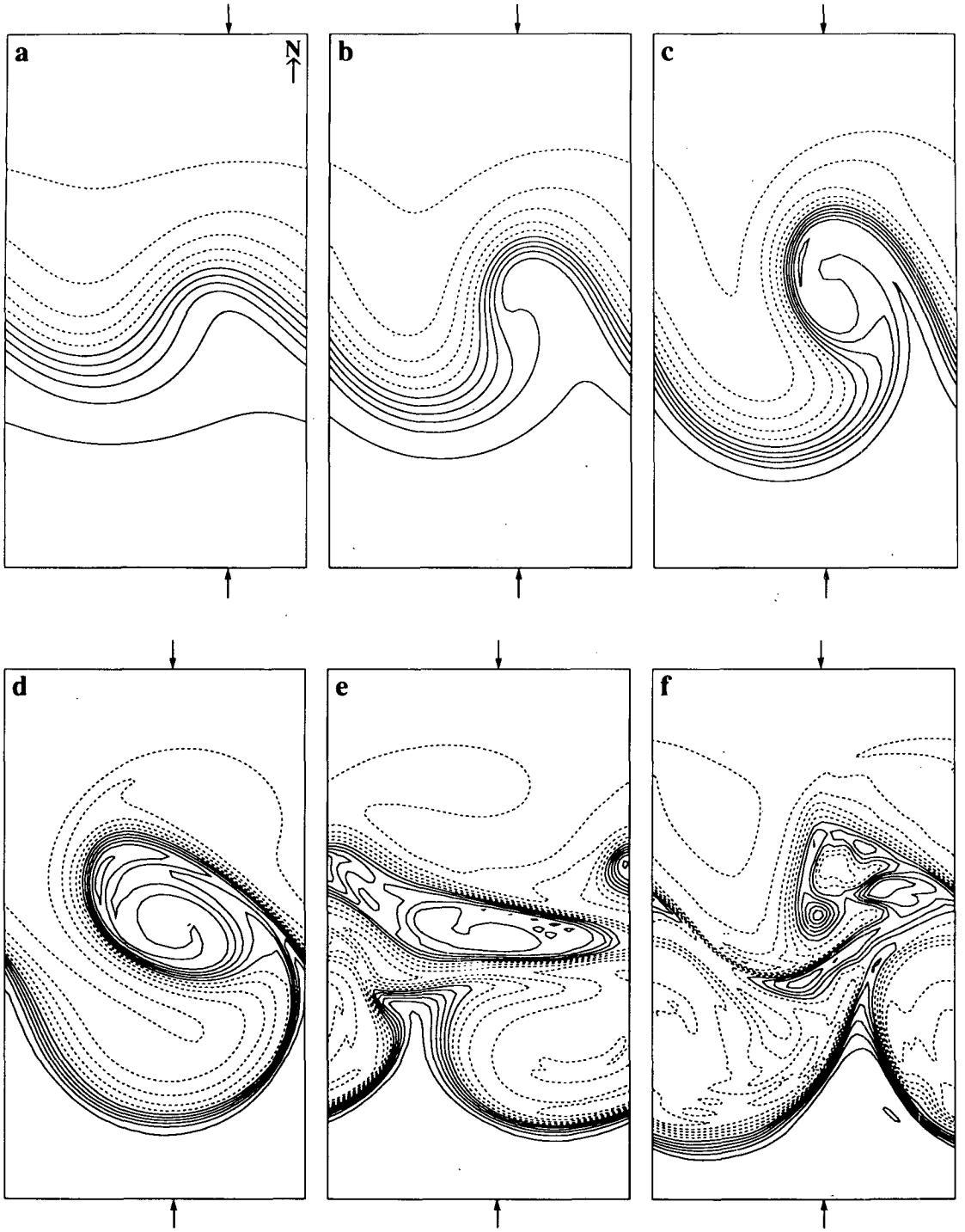

FIG. 6. Surface theta (extrapolated) for HBF run at days (a) 4, (b) 6, (c) 8, (d) 10, (e) 12, (f) 14. Domain is 3103 × 5500 km. Contour interval is 1 K.

previous simulations of nonlinear baroclinic-wave life cycles (prior to our analyses first presented in Peltier et al. 1988, 1990), due to insufficient numerical resolution and/or the inclusion of overly strong dissipative effects, is strikingly reminiscent of the broad spiraling cloud patterns often seen in satellite photographs (Anderson et al. 1969; Scorer 1986, Fig. 15). Corroborating synoptic analyses for a spiraling front are few at this time, perhaps because of the subjective nature of frontal analyses. However, Shapiro (1989) recently observed

a structure remarkably similar to Fig. 6. A sharp warm front appears first, but by day 10, at which time the occlusion is about to be "shed" from the enhanced baroclinic zone; the dominant linear structure might be best described as a single frontal zone deformed by an interior "cusp." Associated with this front at the surface is a zone of low Richardson number (diffusive processes restore the Richardson number to a minimum of 1) and large relative vorticity.

The occlusion that forms is of large horizontal extent. It does not cut off from the main, warm air mass until day 11. By then it is about 2500 km long and 1500 km wide. Wave decay occurs barotropically through horizontal Reynolds stresses. The occlusion becomes zonally elongated and the cold pool to the south moves northward. By day 12 the warm pool is a full wavelength in horizontal extent. The cold pool is then isolated and continues to expand. At day 13 the occlusion has become more elongated and by day 14 substantial intensification of the low has occurred. Note the similar general appearance of Figs. 6c and 6f. Both of these frames correspond to times just prior to a peak in EKE.

A full suite of surface fields is shown in Fig. 7 at day 9.5 or just after the peak in EKE has been reached. Note the finer structure within the larger features of the u, v fields (Fig. 7a and 7b). This corresponds to the smaller scale of regions of pronounced horizontal temperature gradients within the occlusion. The vertical velocity field at a height of 1 km (Fig. 7c) is positive at the "mouth" of the occluding air. This region of rising air extends along the cold front and the warm front. The elongation of vertical velocity contours parallel to the cold front is clearly ahead of the front itself in the position of a prefrontal rainband. Another similar region occurs at the western boundary of the occlusion. The dashed region indicates that fluid is descending from upper levels behind the occlusion. The low level vorticity (Fig. 7d) is largest at the surface front with two maxima near the vertical velocity maxima. Note that convergence near the surface occurs near these two points where flows from the low and high pressure centers meet (Fig. 7f). Figure 7e depicts the potential temperature field. The major axis of the ellipse that defines the occlusion has become more zonally oriented than it was in 6d. Note that a small hook appears in the dashed contour just north of the occlusion. This is due to a developing anticyclonic circulation. The surface pressure and flow field are shown in 7f. The center of the low lies beneath the core of the warm occlusion. A high pressure center has cut off from a ridge to the west.

This rather ideal flow has some features in common with observed cyclogenesis events; namely, the ascent of warm air at the surface into the occlusion and the descent of cold fluid behind the occlusion. Unlike observed atmospheric events, however, (e.g., Carlson 1980) there is no anticyclonic ascent of air originating in the warm sector. More typically the closed high that has formed southwest of the surface low in this simulation is actually found to the southeast so that some warm sector air can flow anticyclonically around it.

2) HBB

The second simulation that we shall describe is of the cyclogenesis event that evolves from a very similar mean state to that described above but here the β-effect is included. This simulation is illustrated by the surface potential temperature fields shown in Fig. 8. Once again cyclogenesis proceeds through to occlusion but now the warm pool is of significantly smaller horizontal scale. At day 9, it measures roughly 800 × 1000 km in the zonal and meridional directions, respectively. Once again the sharpest front is the warm front lying at the neck joining the occlusion to the warm air mass. The typical cusp-like configuration of cold and warm fronts seen on weather maps does not appear until occlusion has occurred (Fig. 8d). Prior to this time the two distinct frontal features are not joined. After occlusion the front translates independently of the occluded cyclone. By day 9 the Richardson number has dropped to 1.5 at the northern warm front. The relative vorticity has become comparable to f_0 prior to day 6. Thus, for an adequate description of the occlusion process, quasi-geostrophic dynamics are clearly insufficient. Note that the occlusion occurs in the northern half of the domain. The northward movement of the wave (Figs. 8a–c) is somewhat surprising since intuitively one might expect that the meridional restoring force present on the β-plane would restrict meridional motion of the perturbation. Cold air does not extend as far south as it did in HBF. The warm pool cuts off sooner and is prevented from becoming as extensive as that which developed in the HBF simulation. After the warm pool has detached, a sharp shallow front with a cusp remains to the south as in HBF (Figs. 8d–f). Similarly, on the upper lid (not shown), a sharp shallow front remains at the north. The central latitudes have become less baroclinic but the temperature gradient has been displaced to the north and south of the largely barotropic occlusion (see below). The initial horizontal temperature structure cannot be erased by diffusion in a dry inviscid atmosphere. The finite meridional scale of baroclinic instability and the existence of regions north and south of the occlusion that remain at their initial temperatures dictate that the initial north–south temperature difference be maintained in two narrow baroclinic regions to compensate for the barotropy of the occlusion.

The evolution of the surface pressure field and horizontal flow vectors corresponding to the times in Fig. 8 is presented in Fig. 9. A closed low pressure center does not develop until day 7 (Fig. 9b). Rapid deepening occurs between days 7 and 9. A small closed low in the center of the domain developed in association with the neck of the occlusion (see Fig. 8d). It has increased

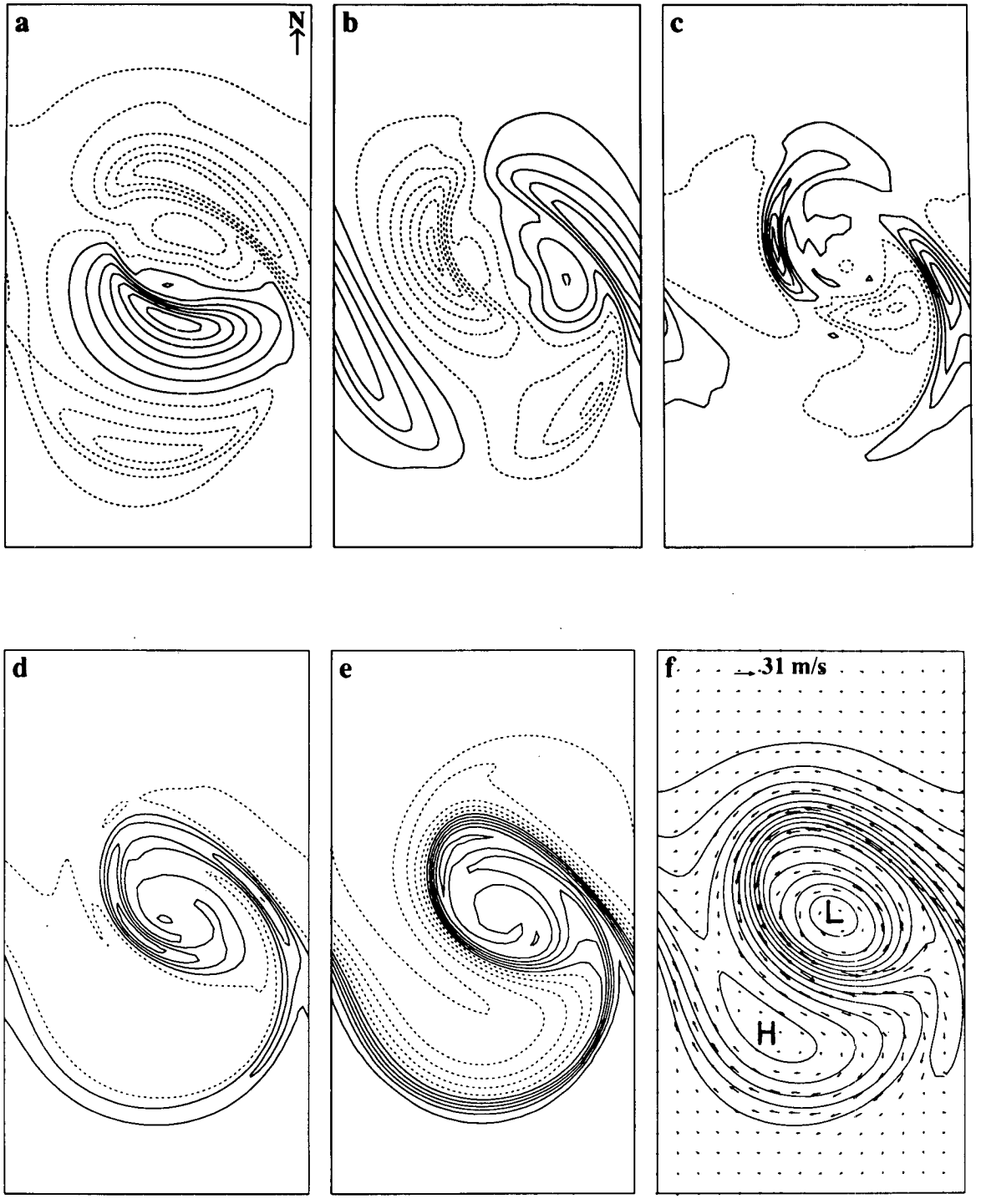

FIG. 7. Low level fields for HBF at day 9.5 at 0.25 km elevation in a, b, d, e, f and 1 km in c. The abscissa is the $+x$ direction and the ordinate is the $+y$ or meridional direction. (a) Zonal, (b) meridional, (c) vertical velocities, (d) relative vorticity, (e) potential temperature and (f) pressure and uv flow vectors are indicated. Contours are every 4 m s^{-1}, 4 m s^{-1}, 0.2 cm s^{-1}, 0.5f_0, 1 K, 2 mb.

in strength by day 12 (Fig. 9e) but has merged with the larger occlusion by day 13. In Fig. 9e a pressure trough has developed, and in Fig. 9f it appears separated from the occlusion. It is this event that is responsible for the slight peak in EKE at day 12 and its subsequent development has been influenced by the presence of the northern wall. However, this simulation was continued in order to document the formation of a sec-

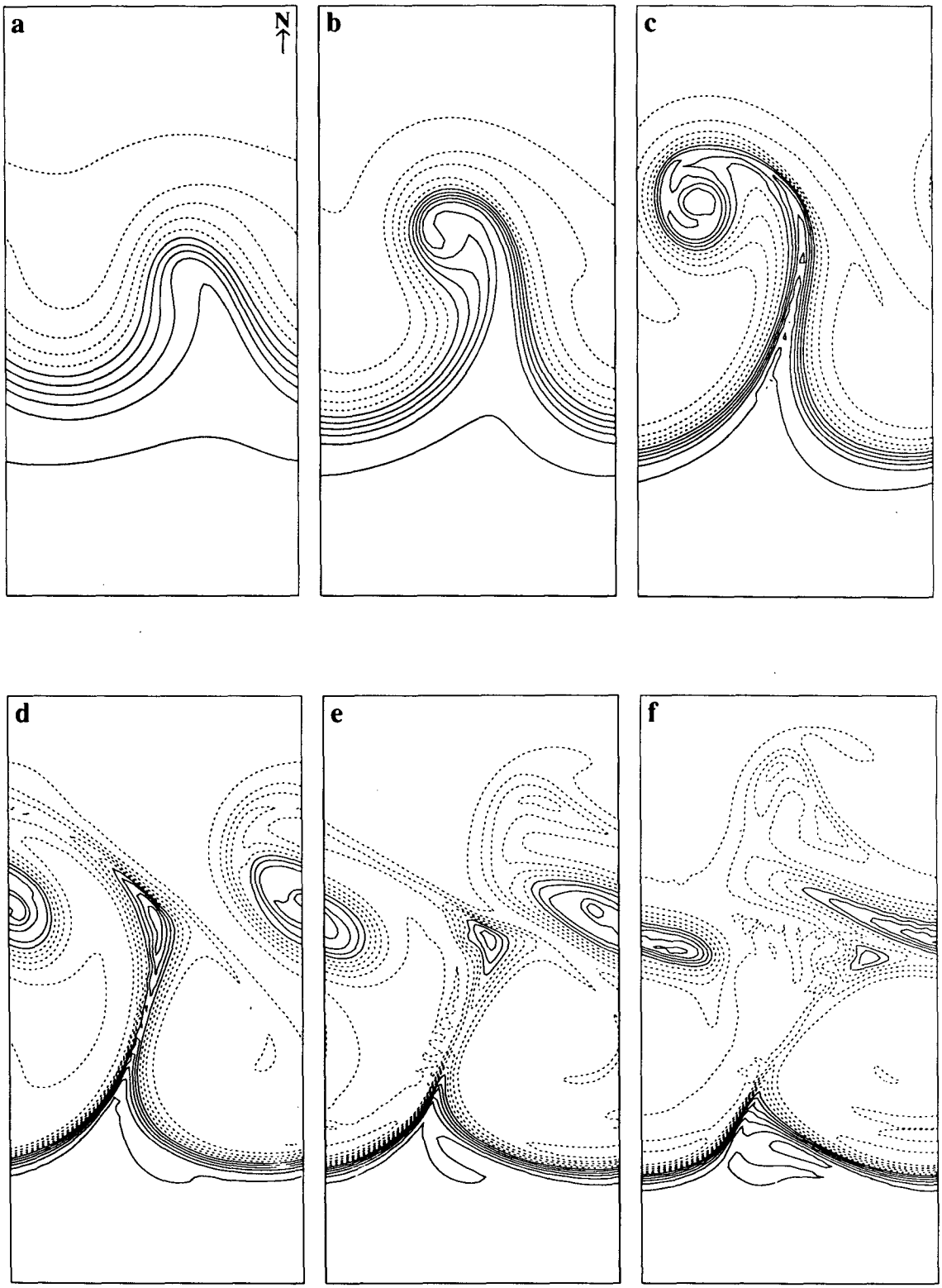

FIG. 8. Surface theta fields (extrapolated) for HBB at days (a) 5, (b) 7, (c) 9, (d) 11, (e) 12 and (f) 13. The domain is 2793 × 5500 km. Contour interval is 1 K.

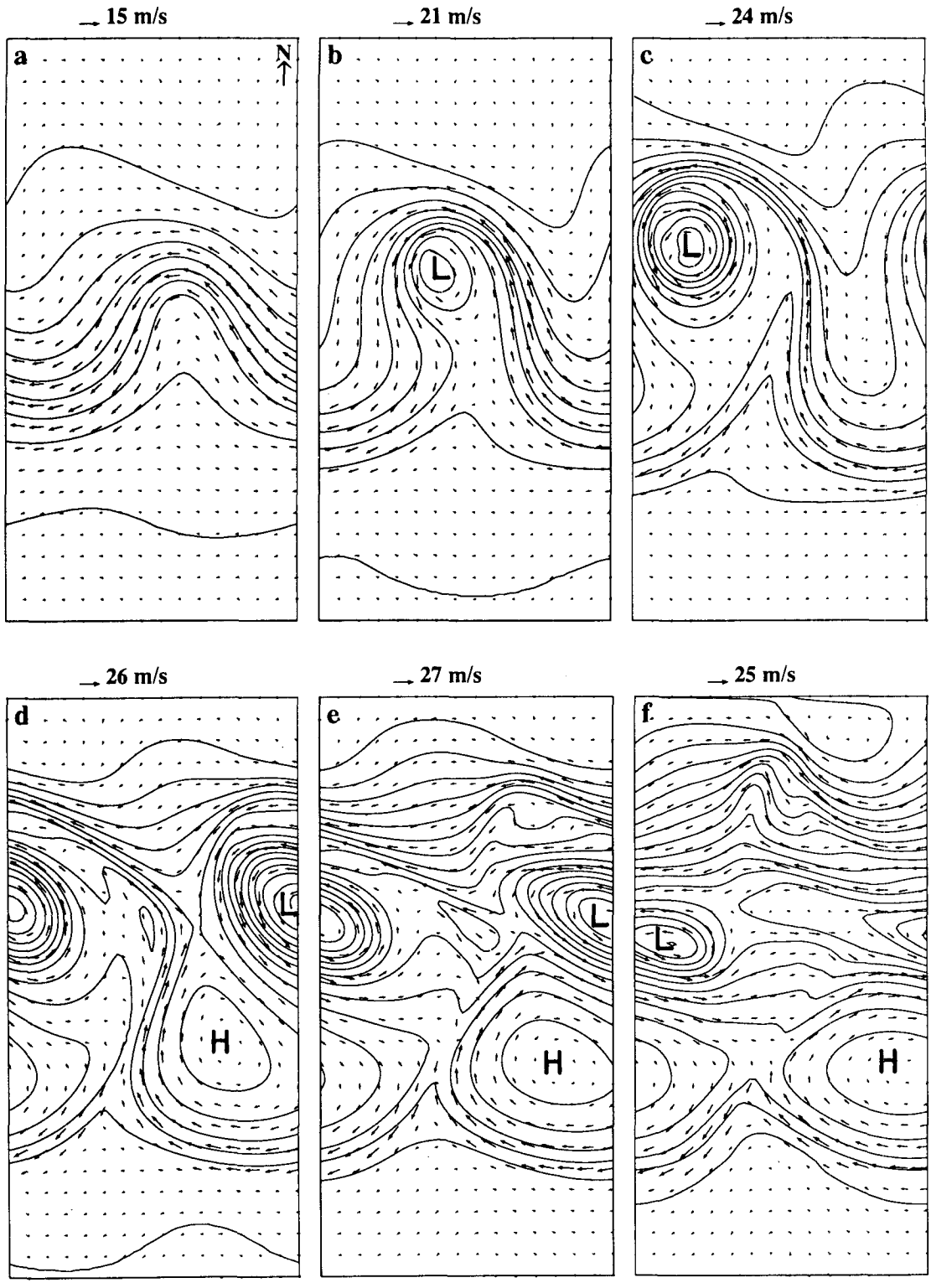

FIG. 9. Pressure and flow vectors for HBB at same times as in Fig. 8. Contour interval is 2 mb.

ondary cyclone on the surface cold front, far from the northern wall. The spontaneous development of secondary cyclones along the surface fronts will be discussed in a companion paper. Note that the final rise of EKE was not observed in the corresponding high resolution simulation, HBBH.

In Fig. 9c a deformation zone is seen to have formed near the center of the frame. The axis of dilation is directed along the cold front. As the high develops the axis tilts NE–SW and becomes an axis of convergence further north (Fig. 9d). This configuration of deformation zones (one at the northern limit of the occlusion, the other along the cold front) is reminiscent of the sharp boundaries of the comma shaped cloud pattern associated with midlatitude cyclones (Carlson 1980; Weldon 1979). Indeed the low-level vertical velocity pattern (not shown) has a clearly defined comma shape. In the previous HBF simulation at day 10, a deformation zone is also present but its orientation is roughly 8 degrees from being N–S. In contrast to this, in the HBB simulation at day 11 the axis is roughly 23 degrees from N–S because the cold high has formed further north. Because of the more southeasterly position of the high, the simulation on the β-plane produces more realistic cyclogenesis in the sense that the vertical motion field takes on the classical comma-shaped pattern not seen in HBF.

After the primary cyclogenesis event, the high strengthens but not so significantly as it did in HBF. Furthermore, the low does deepen again near day 16–17. In the time interval between day 12 and 13, anticyclonic flow has been shed from the northern edge of the occlusion. It soon reaches the rigid boundary and, hence, further consideration of its evolution is impossible due to the artificiality of this boundary condition. This part of the flow appears unaffected by the HRS, which is shearing the main occlusion. Instead, the anticyclonic flow begins to develop. In Fig. 8f, it will be seen that after the cyclone has occluded, the remaining neck of warm air also detaches.

3) HWF

As noted previously, cyclogenesis occurs much more rapidly due to the increased baroclinicity of this mean state at the initial time. The growth rates predicted by linear theory are large, hence the wave should enter the nonlinear regime more quickly. Asymmetries introduced by nonlinearities are well in evidence by day 3. Figure 10 illustrates the evolution of the HWF initial state in terms of a sequence of potential temperature fields. As in HBF an extensive occlusion forms. The low–high axis at the time of peak EKE is 30 degrees from being N–S; i.e., there is an increase in the tilt above that which obtains in HBF and HBB. Note also the difference in orientation of the occlusion between HBF and HWF (Figs. 6d and 10c). The neck of the occlusion is oriented N–S in HWF but almost NW–SE in HBF. Since the ambient low level flow was initially easterly in HBF, the extrusion of warm air took place on an axis with an easterly component. The occlusion here is also zonally stretched and exceeds one wavelength by day 8. The HRS is apparently unable to induce an occlusion that is as oblong as that realized in HBF. Once again there is a similarity between Figs. 10c and 10f. Again, both flow configurations correspond to an instant several hours prior to an EKE peak. The cold air has been able to penetrate quite far south, reaching the southern wall by day 9. Fine structure in the theta field is apparent along the cold and warm fronts in (c)–(f) and is likely due to the increased baroclinicity of this run.

4) HWB

In Fig. 11, which presents a time sequence of surface theta fields for the HWB simulation, we see that the occlusion develops significantly more slowly than that of HWF. Strong frontal asymmetry is apparent by day 3. Fine structure is apparent along both cold and warm fronts as in HWF. By day 6, cold air is beginning to sweep out what appears to be a very small occlusion. However, by day 7 a large occlusion has developed and is composed of colder air than was the case in either the HWF or HBB simulations. It has formed farther north than that in HWF but does not appear any smaller in size. Because the ambient flow is westerly, the flow impedes the westward propagation of the developing occlusion in some regions and allows more air to be entrained within it. However, the strength of the westerlies at the southern edge of the low, where cyclonic flow is also westerly, causes rapid cutoff from the main, warm air mass. Thus, the occlusion is composed of colder air relative to the warm air mass than was the occlusion in HBB. The influence of β has not produced an occlusion of reduced scale for this initial flow as it did for the HB mean flow. Because the formation of the occlusion is clearly a nonlinear process, the expectation of a linear relation between the magnitude of the β-effect and the scale of the occlusion would be unwarranted. Zonal shearing of the occlusion by day 9 also drives the occlusion farther south. Compared to HWF, the remaining front in Fig. 11f is farther north.

Figure 12 compares the development of the low and high pressure centers for HWF and HWB. The pressure patterns associated with HWF and HWB are both characterized by a marked asymmetry of the lows and highs. A maximum pressure drop of 60 mb is obtained. In contrast, the maximum pressure drop (rise) for the low (high) is -20 (10) mb for HBF and -14 (6) mb for HBB. The development of the low and high was simultaneous, the maximum pressure difference occurring at day 7 for HWF (day 8 for HWB) when EKE was a maximum. The low in HWF weakens immediately following that time and remains remarkably steady. In fact the low did intensify (considering the number of closed contours) but the minimum pressure in the low did not change. In contrast, the low in the HWB simulation weakens before redeepening.

Because of the high resolution, the low level vorticity pattern remains coherent through much of the simu-

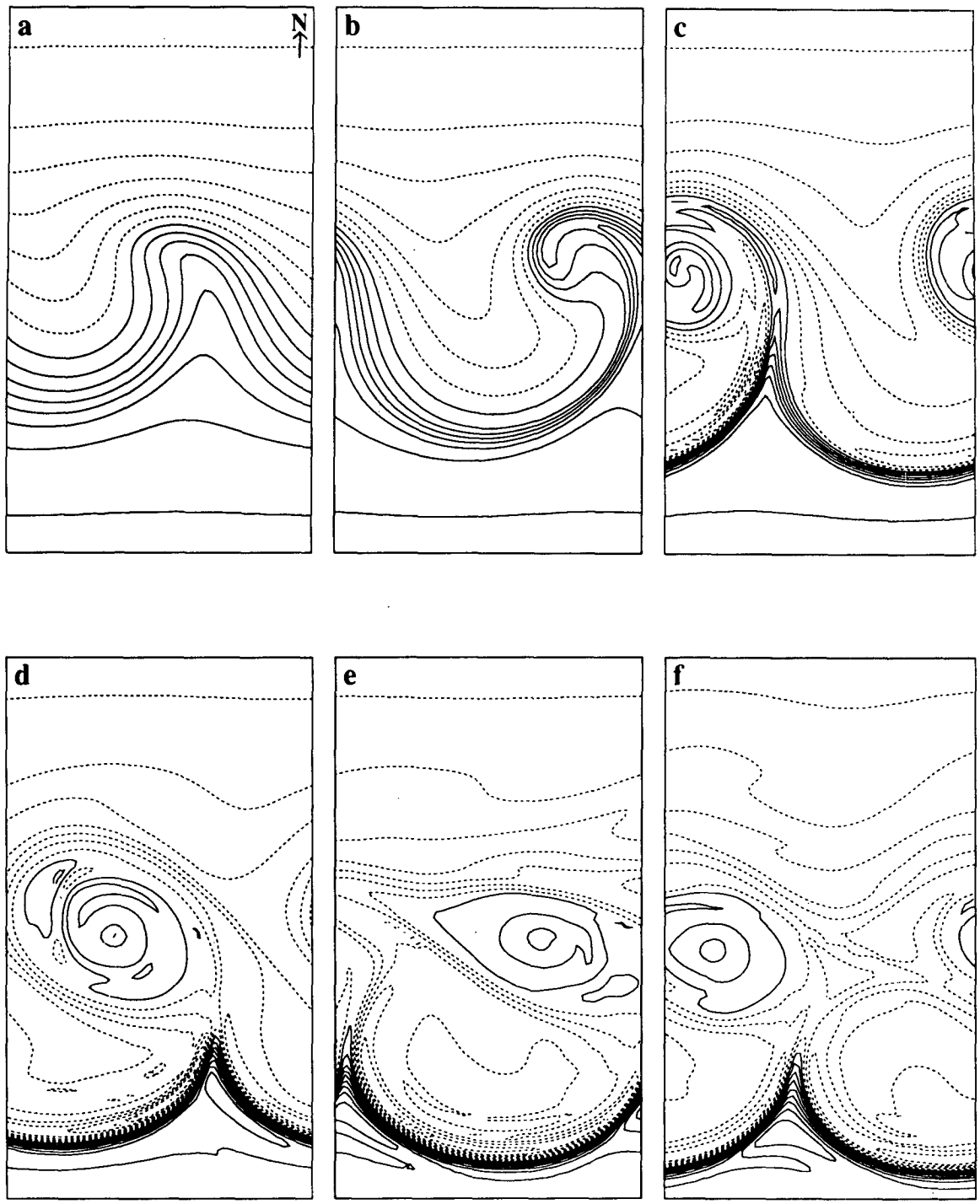

FIG. 10. Theta fields (extrapolated to the surface) for HWF for days 4, 5, 6, 7, 8, 9 in (a)–(f). Domain is 3142 × 5500 km. Contour interval is 2 K.

lation (Fig. 13). Large vorticity is coincident with the spiraling front. A comma-shaped pattern is seen in (a)–(c) and a spiral is apparent in (d) and (e). Comma shaped clouds are often associated with developing cyclones and spiral cloud patterns are often observed with occluded cyclones over the ocean (Anderson et al. 1969; Fig. 15). The vorticity maximum occurs at the mouth of the occlusion and in the northwestern section. Both maxima are associated with low level convergence. The vorticity maximum coincides with the center of a deformation zone whose dilation axis lies along the cold front. Note that the anticyclonic vorticity also

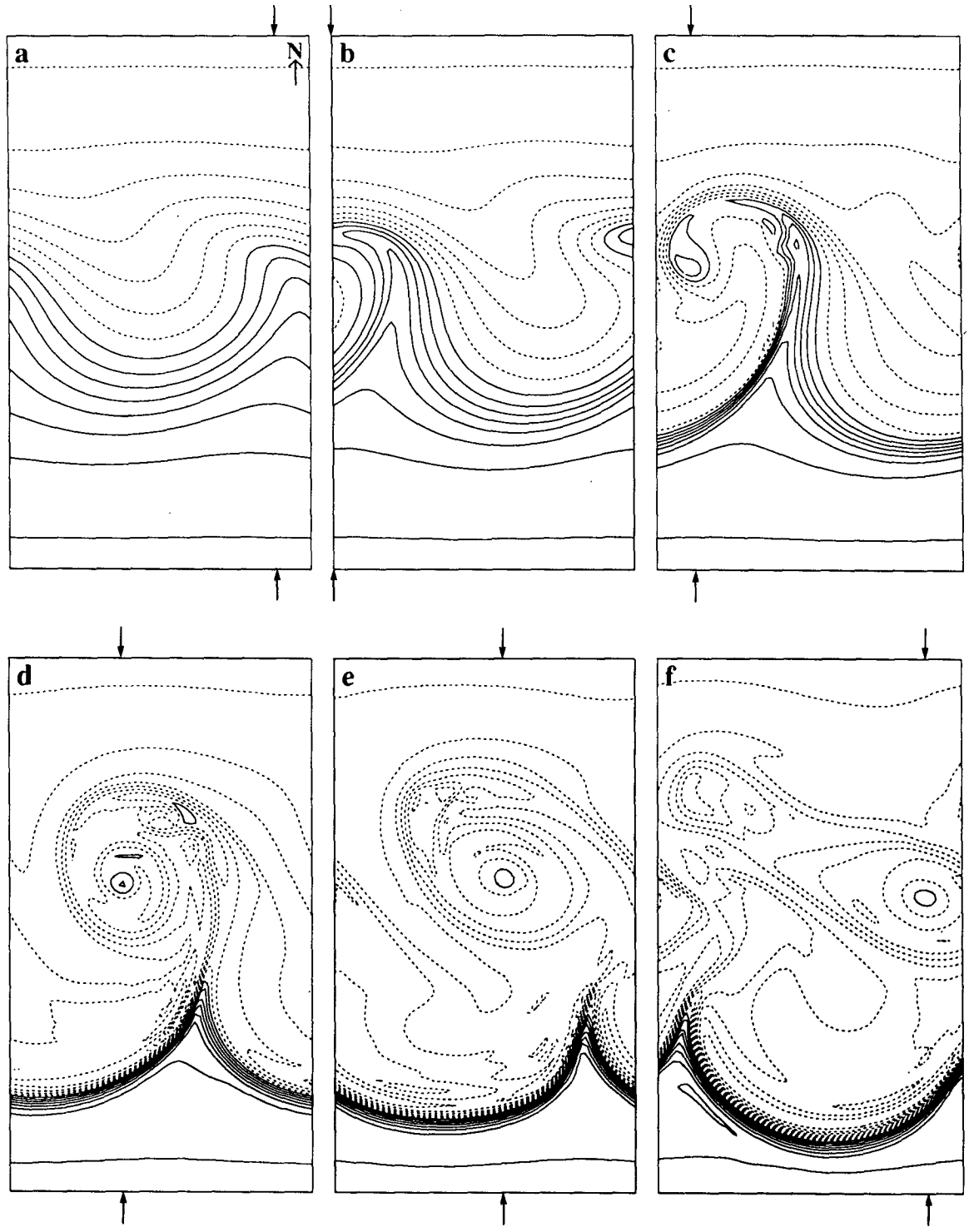

FIG. 11. Theta fields (extrapolated to the surface) for HWB days 4, 5, 6, 7, 8, 9 in (a)-(f). Domain is 3142 × 5500 km. Contour interval is 2 K.

spirals around the low pressure center. With increased resolution the vorticity maximum (minimum) jumps from being $6f_0$ ($-3f_0$) to $11f_0$ ($-4.5f_0$) where f_0 is the Coriolis parameter at the central latitude. Note that there is no restriction on the minimum absolute vorticity for primitive equations dynamics as there is in semigeostrophic dynamics. However, the low level vorticity extrema are unrealistically large due to the highly idealized (frictionless, adiabatic) nature of the flow.

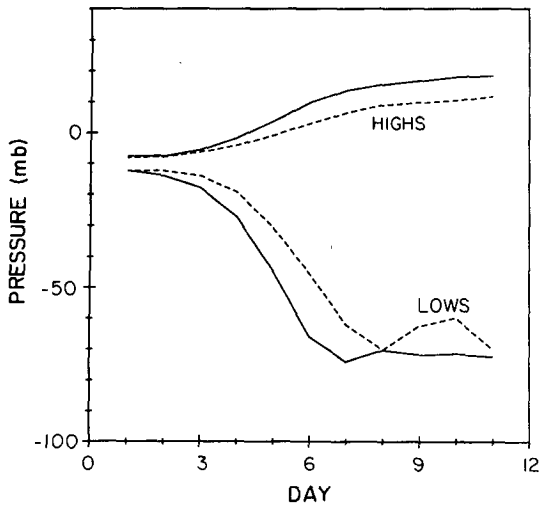

FIG. 12. Evolution of the high and low centers in the HWF (solid) and HWB (dashed) runs.

We have chosen to show the HWBH vertical velocity field because of the better definition of the features we will be discussing. However, all these features were seen in HWB also. The vertical velocity for HWBH (Fig. 14) shows a similar development to the vorticity until day 7, after which much fine structure appears. Both simulations HWB and HWBH display similar fine structure. Within the occlusion, regions of rapidly rising air are adjacent to those with descending air. Clearly such a pattern may be caused by insufficient resolution (vertical or horizontal), though the similarity between HWB and HWBH tends to rule out the latter. However, if this pattern is realistic then the enormous difficulty of forecasting rainfall may clearly be related to the fine horizontal resolution required. In Fig. 14d, the prefrontal and cold frontal bands of rising air (e.g., Houze and Hobbs 1982) are long and clearly defined in the forked solid contours in the south. These bands alternate with bands of descending motion immediately to the northwest. After occlusion (Fig. 14f) the prefrontal band dissipates but the cold frontal band remains. Bands are also apparent within the occlusion. They define a spokelike pattern of alternating rising and descending (internal wavelike) regions. This is best seen in (d) and (e). This pattern is also seen in HWB but is not as well resolved. Such bands of rising motion are sometimes seen in satellite photos (Anderson et al. 1969; Scorer 1986) as cloud bands associated with precipitation within the occlusion. The persistence of the fine structure such as the spoked bands and the multiple comma tail were demonstrated by the appearance of the latter in HBB and in both high resolution simulations, and the appearance of the former in high and low resolution simulations. The occurrence of these patterns for differing resolutions indicates that the role of diffusion (which is affected by resolution) is not crucial to their existence.

For comparison, the visible imagery of a storm that occurred over the western Atlantic is shown in Fig. 15. The general cloud pattern is quite similar to that of Fig. 14c. In addition, the spiraling cloud bands within the occlusion in Fig. 14d bear a striking resemblance to those in Fig. 15. The multitailed pattern of the cloud field is also evident in Fig. 14c,d,e. The degree of similarity obtained without the inclusion of any moisture is somewhat surprising. However, the cloud bands within the occlusion (Fig. 15) are not deep. Thus, the shallow bands may well be regarded as passive tracers indicative of the velocity field. Then the similarity between our simulation and the observation is more than coincidental and suggests that some of the observed mesoscale features of midlatitude cyclones may be understood on the basis of dry dynamics alone.

The midlevel flow (not shown) for HWB indicates that the surface low has formed east of the midlevel trough (i.e., the low tilts north and west with height). However, by day 6 the surface low is virtually beneath the midlevel low but is slightly south and east of it. Thereafter, the low centers are exactly coincident. A ridge of high pressure exists to the east, sharpening at day 7 before the HRS peak is reached on day 8. At day 9, the ZKE peak is reached and the trough has weakened. An anticyclone in the north appears to have cut off from a tilting ridge extending NW–SE. A similar but weaker circulation is observed at the surface northern boundary. The midlevel vorticity pattern is roughly comma shaped. Values as high as $3f_0$ are achieved. The vertical velocity pattern is also similar to the surface pattern except that maxima are shifted to the north and west until day 7 when the velocity pattern is largely vertically oriented. The spatial pattern is fine structured from day 7 onward. Rising motion corresponds to the cold front and the northern half of the occlusion, implying that these motions are deep.

Depicted in Fig. 16 is the potential temperature field superposed upon the uv flow vectors at a height of 4 km corresponding to the same times as illustrated in Fig. 11. Cold advection along the trough and warm advection along the ridge are apparent in (a) and (b). In (c) cold advection occurs south of the occlusion and warm advection occurs as air flows anticyclonically across the ridge to the east. The flow is well aligned with the isentropes in (d)–(f) except in the north in (f) where the boundary influences a cyclonic and an anticyclonic circulation. This illustrates the pronounced barotropy of the flow in (d)–(f).

A series of north–south vertical cross sections of the θ field through the HWB domain (as indicated by the arrows in Fig. 11) is shown in Fig. 17. South appears on the right side of each frame. In (a) the northern warm front is apparent at the surface. In (b) the cold air has appeared south of the low as indicated by the appearance of a dashed contour. At the upper lid, warm air has appeared north of the low. This is indicated by the minimum slope in the contours at upper levels. In

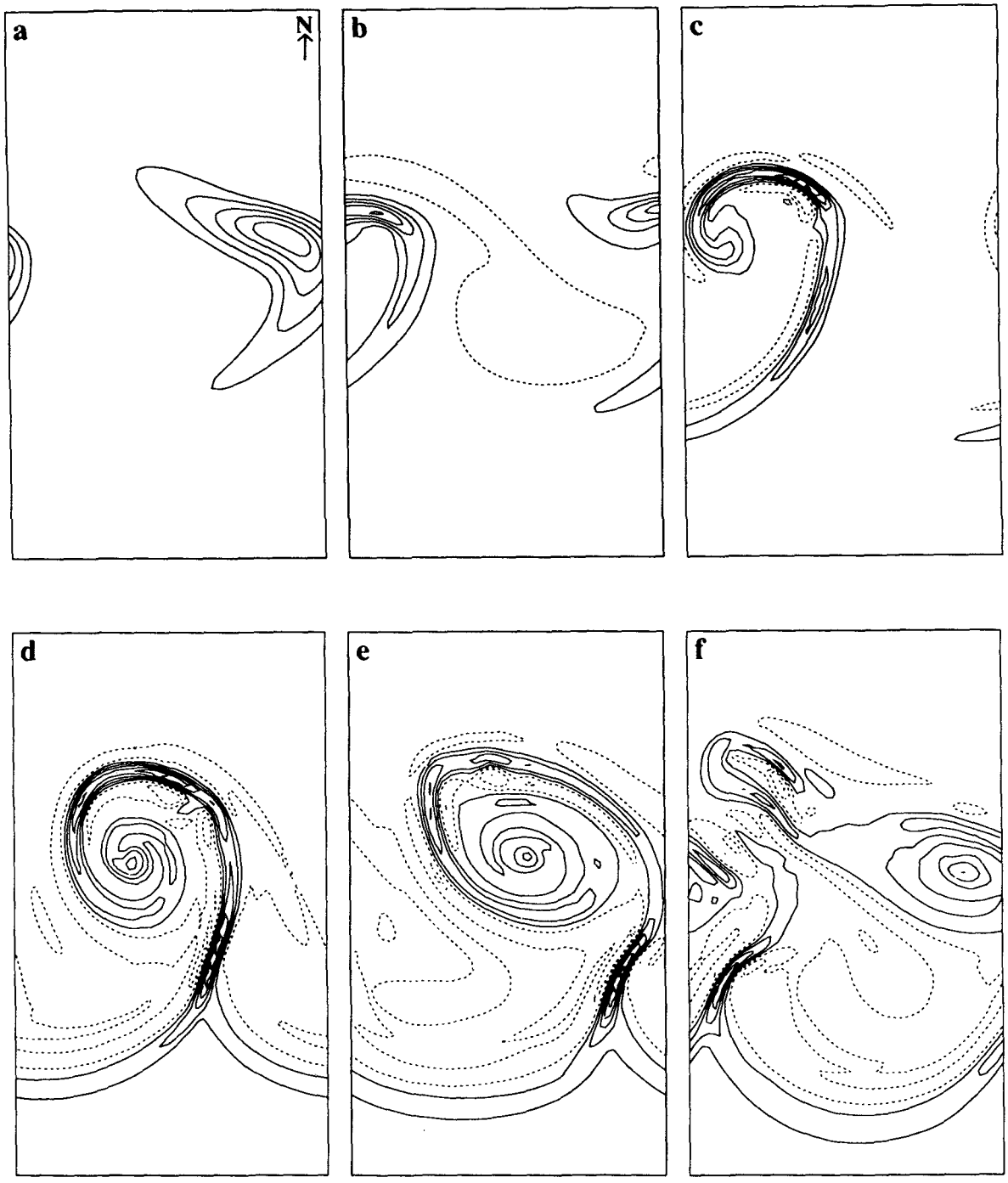

FIG. 13. Relative vorticity at 0.25 km elevation for HWB days 4–9 in (a)–(f). Contours are given every $0.1f_0$, $0.5f_0$ in (a) and (b) and every $1f_0$ in (c)–(f) where $f_0 = 10^{-4}$ s^{-1}.

(c) the surface cold pool is seen extending southward creating a shallow, sharp front. A second cold pool associated with spiraling air in the low is evident just south of the most northern front. The cold pools are seen as the maxima in the slope of the contours near the surface. The sharp peaks in the middle of (d) are due to the rapid small-scale temperature gradients in the spiral. Cold air has begun to replace warm air at the surface. This is seen by comparing the heights of the lowest solid contour in (c)–(f). In (e), which is at the time of HRS maximum, the upper and lower disturbances are vertically aligned. The lower level tem-

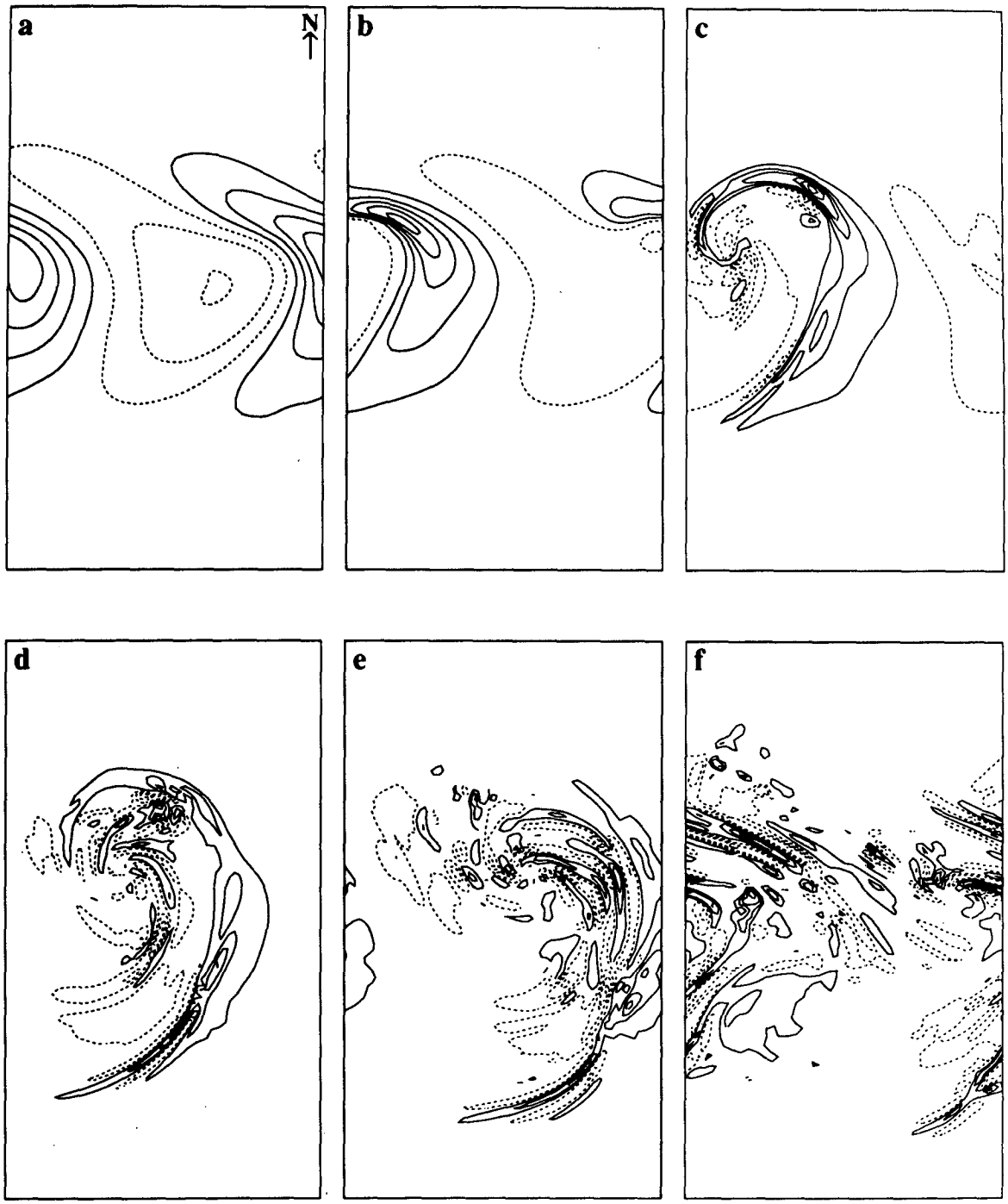

FIG. 14. Vertical velocity 1 km above surface for HWBH for the same times as in Fig. 11. Contour intervals are (0.2, 0.5, 1, 2, 2, 2) cm s^{-1} in (a)–(f), respectively.

perature is becoming increasingly cold near the center of the low. In (f) the low centers are still vertically aligned but warm air (above 0°C) has been almost entirely removed from the surface. Thus, the occlusion appears to be lifting off the surface even in this dry, nearly inviscid, simulation. With surface friction included this lifting may be more rapid. In contrast to the suggestion of the polar front model, however, lifting occurs after the occlusion has separated from the main warm air mass.

5) SUMMARY

In summary, we have seen that cyclogenesis proceeds through to occlusion for all of our simulations. This process is greatly influenced by the nature of the state

in which the initial baroclinic instability occurs. Cold and warm fronts arranged in a cusp-like formation as described by the Polar Front theory (Bjerknes 1919; Bjerknes and Solberg 1923) do not appear early in the evolution of the nonlinear waves. Instead, a warm front at the leading edge of the cyclonically turning warm-sector air forms first. Fluid descends from mid to upper levels and turns anticyclonically west of the surface cold front. The cold front then intensifies as a result of this anticyclonic flow. The occlusion occurs as warm sector air is pinched into a pool, remaining attached to the southern warm air mass by a thin neck of warm air. This neck is thinned by the developing anticyclonic flow and the cold front appears to overtake the warm front. When the two surface fronts intersect the warm pool separates. The beginning of the occlusion phase is marked by the vertical orientation of the low pressure center. The end of the occlusion phase occurs with the detachment of the cyclone from the warm air mass to the south. In all cases, an anticyclone forms south of the occlusion at the surface and a second develops north of the occlusion on the upper lid. Thus, the process of cyclogenesis involves the development of anticyclones. This suggests that cyclogenesis may perhaps be better understood in the context of the vortex pair. Observations indicate that sometimes this is indeed the case (Boyle and Bosart 1983, 1986). After the occlusion has occurred the pool persists, decaying in intensity and becoming zonally elongated. Barotropic conversions dominate in this stage. Further deepening of the low or filling of the high may occur but the high always increases in meridional extent. Further reintensification

FIG. 15. Visible imagery of a storm that occurred at 1147 UTC 12 August 1985 in the western Atlantic Ocean. The outline of the Canadian Atlantic provinces are dotted and appear in the northwest corner.

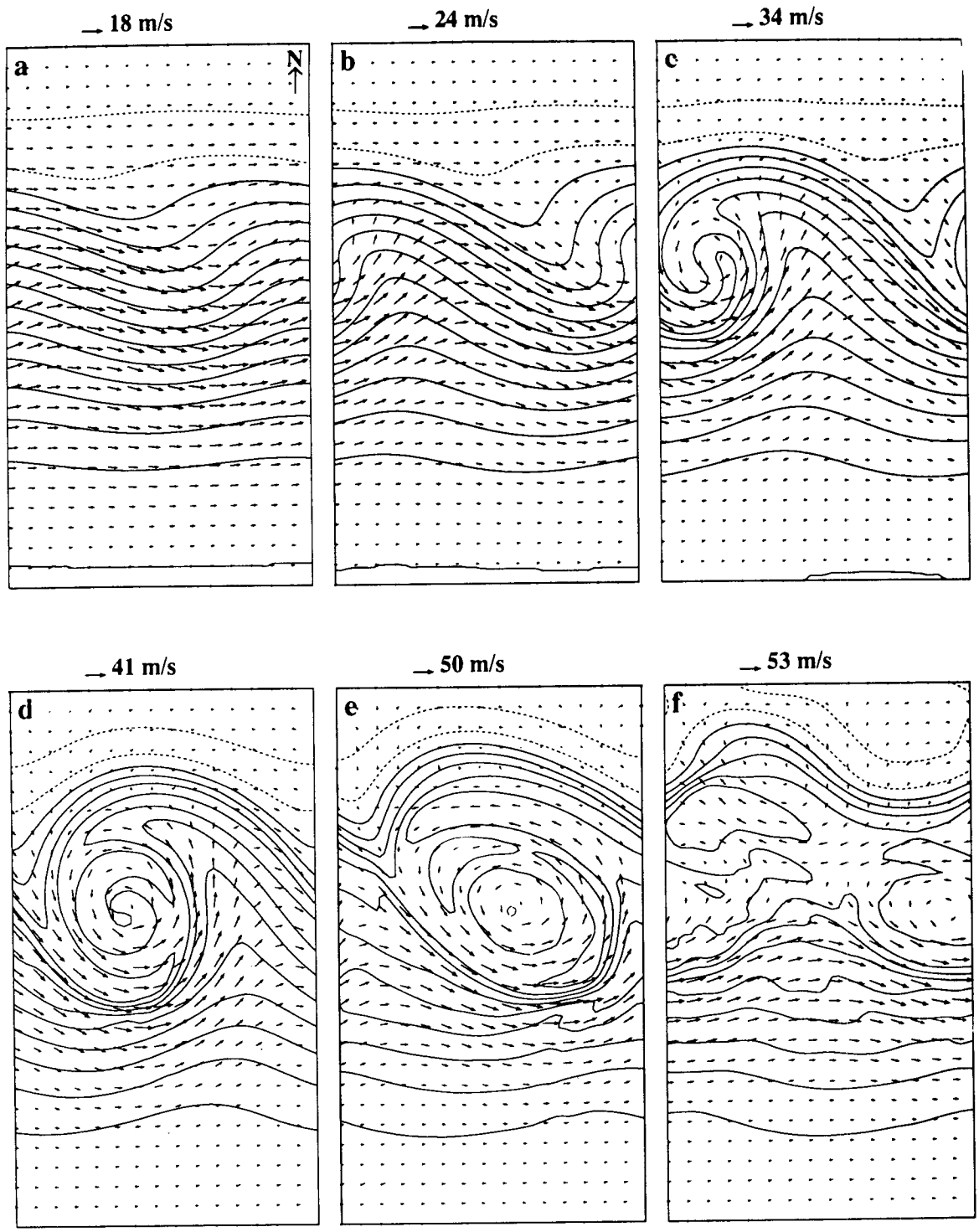

FIG. 16. Midlevel (z = 4 km) potential temperature and flow vectors for HWB at the same times as in Fig. 11. Contours are given every 2 K.

of the low or high is usually due to both baroclinic and barotropic conversions of energy. Because of the rigid lid and the absence of a stratosphere, cyclogenesis occurs on the lid as well except that here it is the cold air that more rapidly intrudes into the warm air. The effect of cyclogenesis on the mean flow is to produce easterly–westerly–easterly jets on the lower surface and westerly–easterly–westerly flow on the lid (the details of the

wave–mean flow interaction will be discussed in a later publication). The greatest change occurs at lower levels. Overall, the warm air south of the central latitude has been cooled and the cold air to the north has been warmed.

c. *Frontogenesis*

It is through an examination of the symmetry of the cold and warm fronts that we can best illustrate the influence of the beta effect on the dynamics of the baroclinic systems that we are in the process of studying.

First, we shall provide some necessary clarification on the subject of nomenclature. Traditionally the surface cold front appears on the western edge of the warm sector air and the surface warm front on its eastern edge. Here, as in Mudrick (1974) and Takayabu (1986) the front at the leading edge of the cyclonically turning warm air forms first. This is the warm front. Following the appearance of this feature, the cold front proceeds to sharpen. In cases in which the ambient low level wind is easterly (i.e., HB mean states) the cold front is on the eastern edge of the warm sector air. Nevertheless, we will refer to this as the warm front in keeping with the usual schematic model. In the interest of clarity we shall denote the northern warm front as LWF (leading warm front), the front on the western edge of the wedge of warm air as the TCF (traditional cold front) and the eastern front as the TWF (traditional warm front).

Mudrick (1974) shows that for nonlinear quasi-geostrophic dynamics no LWF appears and the TCF and TWF are similar in intensity but that this "symmetry" does not prevent cyclogenesis from occurring. Instead the low and high are also symmetric and warm air that spirals around the low is mirrored by cold air sweeping into the high. A parallel simulation using the hydrostatic, Boussinesq, primitive equations shows that when the restrictions imposed on the flow by quasi-geostrophic constraints are removed, the symmetry between the low and high pressure centers disappears and only the low features spiraling temperature gradients. This asymmetry also appears in nonlinear hydrostatic semigeostrophic simulations (Hoskins and West 1979;

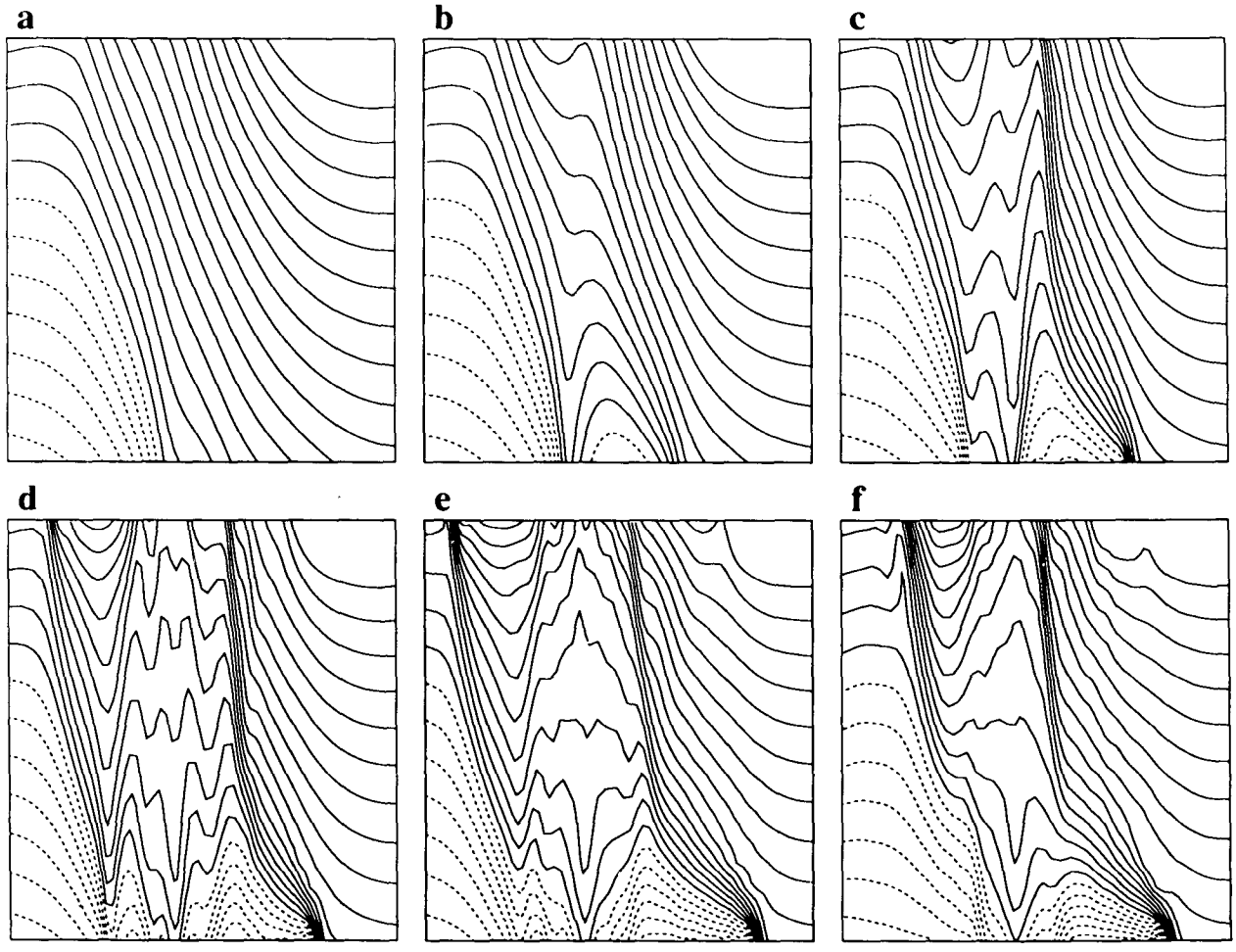

FIG. 17. Vertical cross section at arrows in Fig. 11 of HWB run. Potential temperature contour interval is 2 K.

Hoskins and Heckley 1981). The symmetry imposed by the nonlinear quasi-geostrophic equations can be understood intuitively as follows: given the symmetry of a geostrophic flow with respect to lows and highs, if the model is constrained such that only geostrophic flow is advected by geostrophic flow this symmetry will be preserved. Both advected and advecting quantities have this symmetry. If we begin with an initial state that contains this symmetry then subsequent development will be similarly characterized. This is certainly true of an initial state consisting of a steady, geostrophic flow and a sinusoidal perturbation.

The primitive equations relax these constraints in two ways: 1) by permitting ageostrophic advection and 2) by including vertical advection. The inclusion of ageostrophic advection alone results in simulations that contain asymmetry between the highs and lows as Mudrick's study shows. Our simulations have also included vertical advection and cyclogenesis has been followed through to the end of the occlusion phase. A detailed discussion of the impact of the nonhydrostatic terms in our simulations will be provided in section 5d.

The inclusion of the beta effect also effects a further enhancement of the asymmetry between the LWF and TCF development. Compare, for example, Figs. 6a and 8a and also 10b and 11b. With the beta effect included, the LWF becomes sharper earlier. In addition the TWF is much weaker than the TCF on the β-plane (compare Fig. 6d and 8d and 10c and 11c). In analogy with the inclusion of advection of the ageostrophic flow, incorporation of the variation of the Coriolis parameter allows more asymmetry to develop between lows and highs in the context of primitive equations dynamics.

This asymmetry is best illustrated through an examination of vorticity production. In the anelastic system, the generation of the vertical component of relative vorticity, ζ, is governed by the equation

$$\bar{\rho}\,\partial_t\zeta + \bar{\rho}\mathbf{V}\cdot\nabla(\zeta+f) = -\bar{\rho}(\zeta+f)D + [\bar{\rho}\,\partial_x w\partial_z u - \bar{\rho}\,\partial_y w\partial_z v] \quad (11)$$

(A) (B)

where $D = \partial_x u + \partial_y v$ and where $\mathbf{V} = (u, v, w)$. Term A describes the production of vorticity through convergence and B the production through the tilting of horizontal vorticity into the vertical. Since for the following discussion we will be primarily concerned with a period early in the simulation and since vertical motions are at most 0.02% of the horizontal velocity at any time in any simulation, the influence of (B) is assumed small. Under the quasi-geostrophic (QG) approximation,

$$\bar{\rho}\,\partial_t\zeta_g + \bar{\rho}\mathbf{V}_g\cdot\nabla_h(\zeta_g+f) = -\bar{\rho}f_0 D \quad (12)$$

where $\mathbf{V}_g = (u_g, v_g, 0)$, the subscript h refers to horizontal flow and the subscript g to geostrophic flow. On the β-plane we can write in the QG limit:

$$\bar{\rho}\,\partial_t\zeta_g + \bar{\rho}\mathbf{V}_h\cdot\nabla_h[\zeta_g + \beta(y-y_0)] = -\bar{\rho}f_0 D. \quad (13)$$

Then for a given flow with symmetry of convergent and divergent flow about a central latitude, the vorticity production is exactly equal in magnitude and opposite in sign. Note that this is true of nonlinear flow as well, given the initial symmetry.

Early in our simulations the QG equations are approximately valid for these long wavelength waves. But asymmetry between the warm and cold fronts appears early (day 3 in HWF and HWB, day 4 in HBF and HBB) and in particular before ζ first exceeds f_0. Thus, asymmetries associated with non-QG dynamics become apparent well before QG theory becomes invalid. Because w is still small at this early time in all simulations

$$\bar{\rho}\,\partial_t\zeta + \bar{\rho}\mathbf{V}_h\cdot\nabla_h[\zeta + \beta(y-y_0)] \approx -\bar{\rho}(\zeta+f)D. \quad (14)$$

On the f-plane, asymmetry arises from the fact that vorticity increases only where convergence occurs and vorticity is positive, or where divergent motions and negative absolute vorticity occur. On the β-plane, the vorticity production is greater if convergence and positive vorticity occurs in the north than if this occurs in the south. This bias toward the north explains the enhanced early development of the LWF and the more northern development of the occlusion on the β-plane. As discussed by Takayabu (1986) the difference in strengths of the TCF and the TWF are due to the convergence along the TCF. The enhanced difference between these fronts on the β-plane appears to be due both to the explicit y dependence of the divergence and to the advection of absolute vorticity.

d. Nonhydrostatic and anelastic effects

To our knowledge the simulations reported here are the first for which a nonhydrostatic model has been employed in baroclinic-wave life cycle analyses. Our reasons for employing such a model were to facilitate future research in which we intend to include the influence of moist dynamics and to minimize the assumptions regarding the governing physics. It is natural then to ask to what degree such effects are important on this scale. To that end we have constructed a field which measures the departure from hydrostatic balance, (NH), that has the explicit form

$$NH(x, y, z, t) + \delta_z P' + P'[\overline{g/c^2(z)}^z] - \bar{\rho}^z g\overline{\theta^*}^z = 0$$

where

$$\frac{dw}{dt} = -NH(x, y, z, t).$$

When integrated over the domain (and divided by the domain volume), $\langle\{NH\}\rangle$ is at most 0.001% of the

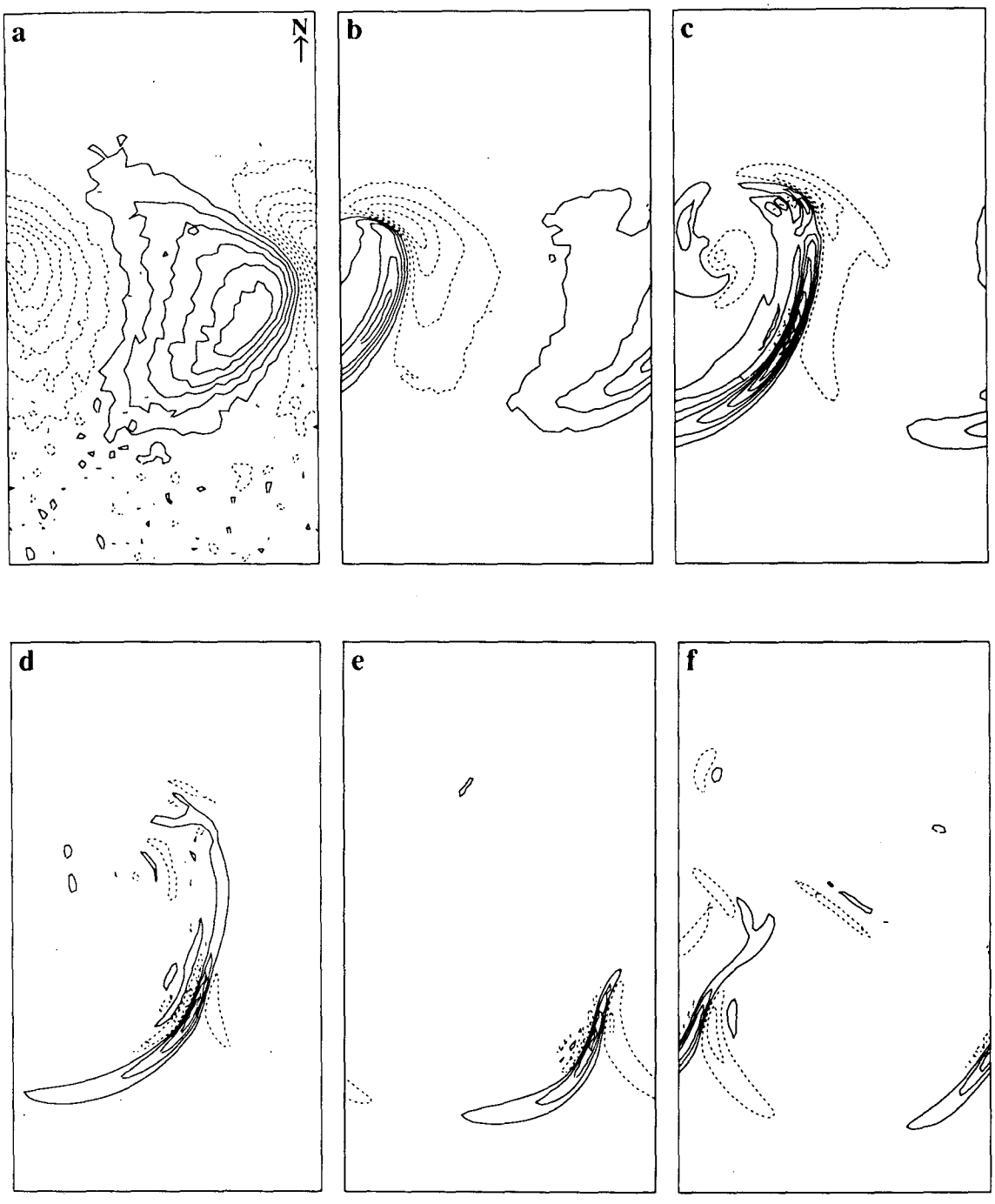

FIG. 18. Nonhydrostatic term at 0.25 km elevation for HWB at days (a) 4, (b) 5, (c) 6, (d) 7, (e) 8 and (f) 9. Contour intervals are 0.1, 0.4, 1.0, 3.0, 3.0, 3.0 mb km^{-1}, respectively.

domain integrated pressure or theta term in (21). This was true of all simulations, with and without horizontal diffusion. It may therefore appear that nonhydrostatic effects are unimportant. Of course this conclusion is a function of the resolution and the diffusion employed. More importantly however, nonhydrostatic effects might be expected to be more significant locally and the small value of the domain integrated field does not address this concern.

The spatial distribution of the field *NH* is shown in Fig. 18 for days 4 to 9 of HWB. The horizontal planforms are shown for the surface since this is the height at which the largest values occur. The roughness of the contours in days 3 and 4 are indicative of the fact that

nonhydrostatic effects in these early stages of the evolution of the disturbance are barely above the noise level. (Only four or five significant digits are retained for plotting purposes.) The pressure and theta term are typically 189 mb km^{-1} averaged over the domain so locally the nonhydrostatic acceleration can be as much as 7% of these terms. Of course if this term is large precisely where the vertical pressure gradient is small, then this would be a grave underestimation. The vertical cross sections through the low centers show negligible vertical gradients in the vicinity of the fronts. Because of this, the ratio of NH to $\delta_z P$ is not well behaved and hence was not directly computed and the underestimation cannot be exactly determined.

The nonhydrostatic accelerations are largest along the surface front and are well correlated with the low level meridional velocity. In the occlusion where the vorticity is high, nonhydrostaticity is not especially important. Hence, it appears that the advection of vertical velocity by the divergent component of the wind forms the largest contribution to NH.

Thus, nonhydrostatic accelerations are locally important even in a dry inviscid atmosphere and are especially important along the neck of the occlusion and the cold front. This is consistent with observations that show the highest cloud occurring in these locations (Carlson 1980). According to Fig. 18 the highest clouds would be predicted to form along the warm front at the neck of the occlusion. This is not surprising since, as we have already seen, this front is the first to form and to develop large low level vorticity. There is also vertical acceleration upward at the mouth of the occlusion, but once the occlusion pinches off (day 7) this has largely disappeared. Behind the cold front it is the descent that produces nonhydrostatic accelerations downward. Ascent occurs ahead of the cold front and is strongest at midlevels. The maximum vertical accelerations occur between days 7 and 8. From Fig. 3 we can see that this corresponds to the primary peak in EKE.

We have not directly considered the comparison of the Boussinesq and anelastic approximations on the evolution of these waves. However, some features of the anelastic solutions are evident. On the f-plane, the synoptic scale baroclinic wave has equal amplitude on both surfaces under the Boussinesq approximation as discussed in *I* but under the anelastic approximation the upper wave dominates. Similar asymmetry was seen in our simulations. The upper cyclone developed slightly more quickly and more intensely than the lower one. Of course on the β-plane this is offset by the much greater influence of the lower level perturbation. Because of the presence of the unphysical rigid lid, realistic upper level motions are not expected here. A more realistic tropopause would dampen upper level motions so that it is expected that the anelastic approximation is preferable to the Boussinesq approximation when accuracy in portraying upper motions is critical.

6. Conclusions

We have performed numerical simulations of the nonlinear evolution of long wavelength baroclinic waves using models with high resolution incorporating nonhydrostatic effects. The anelastic equations were employed in these analyses. As in previous nonlinear simulations performed by other authors we have observed the development of fronts, the leading warm front forming first, and the formation of an occlusion. Unlike previous simulations we were able to resolve the cutting off of the occlusion from the warm air mass. The remaining front has a cusp-like appearance with the cold front being sharper than the warm front. This front propagates independently of the occlusion. As a result of cyclogenesis, westerlies have been strengthened in the center of the meridional domain while at extreme latitudes easterlies have developed. Warm air has been advected northward and cold air has been advected southward.

Features appearing in our dry, inviscid simulations that are in common with observed synoptic scale cyclones are the cyclonically rising warm air at the mouth of the occlusion, the descent of cold air behind the occlusion, the formation of warm and cold fronts in the mature stage and the development of comma-shaped vertical velocity patterns. Long bands of rising motion formed at the surface ahead of and above the cold front. Spokes of alternately rising and descending motions appear in the occlusion. The relative vorticity is largest near the horizontal surfaces along the fronts and in the occlusion forming a sprial pattern.

In two main respects the process of cyclogenesis described here differs from the conceptual model of cyclogenesis known as the polar-front theory. First, the cusplike configuration of warm and cold fronts envisioned by this theory is not seen until the time of separation of the warm cyclonically rotating pool from the remaining warm air to the south. Instead, a warm front forms first at the leading edge of the warm intrusion into the cold air mass. The cold front intensifies only with the descent of upper level fluid since this descent creates a shear zone whose axis lies along the cold front. In this respect, all other simulations of idealized three-dimensional nonlinear baroclinic wave development employing non quasi-geostrophic dynamics concur. Second, the process of occlusion is not seen to occur as a removal of the warm sector air from the surface, as the polar-front theory suggests. Instead, the surface warm sector air rotates cyclonically about a tongue of colder fluid, creating spiraling fronts. Occlusion begins when vertical alignment of the low pressure center is achieved. The occlusion process occurs as the developing anticyclonic flow south of the cyclone restricts the northward flow of air creating a narrow "neck" or "cord" attaching the cyclone to the warm air mass. Since the eastern and southern edges of the anticyclone coincide with the surface cold front, the

latter is seen to "catch up" with the warm front. Occlusion is completed with the separation of the warm pool from the warm air mass. Since no previous simulations have fully described the details of the occlusion process, comparison with the work of others is not possible. Nevertheless, the beginnings of a similar occlusion process were seen in many previous simulations (Mudrick 1974; Takayabu 1986; Hoskins 1983; Golding 1984; Simmons and Hoskins 1978; Keyser et al. 1989). In the light of these discrepancies, modifications to the conceptual polar-front model are advocated: (i) A recognition of the leading warm front's existence in the developing cyclone, (ii) an expectation of warm and cold fronts intersecting in the typical cusp formation seen on synoptic weather charts only after occlusion, and (iii) the prediction of an occlusion at low levels in the cold fluid side of the cusp-shaped front. The occluded warm pool is seen to be a long-lived "coherent structure" for dry, inviscid adiabatic motions. Naturally, these modifications must be verified first from the observational standpoint. In this regard, the current work of Shapiro and Keyser (1990) supports our view.

Qualitative differences are apparent between simulations performed on an f-plane and those performed on a β-plane. As pointed out in Peltier et al. (1990) we envision a clear analogy between the process of baroclinic wave occlusion in the atmosphere and the process of Gulf Stream ring formation in the oceans. On the β-plane the leading warm front develops sharp gradients more quickly. Also the difference in intensity between the cold and warm fronts defining the wedge of warm sector air is enhanced. The occlusion is seen to form farther north in the domain with the inclusion of the β-effect. This northward movement of the wave on the β-plane indicates nonlinearity and implicitly, the increased importance of wave–wave interactions. The simulations on the β-plane were observed to have short periods of linear wave growth (less than 1 day).

Nonhydrostatic effects can be very important locally and are most prevalent where the leading warm front and the cold front intersect the boundaries. We estimate (conservatively) that nonhydrostatic effects can be as large as 7% of the pressure gradient locally in the dry dynamical system. We expect that the inclusion of nonhydrostatic motions is important in order to obtain quantitatively satisfactory results in these sensitive regions of the flow.

Finally, the energetics reveal quasi-regular oscillations to be characteristic of the nonlinear life cycle only for simulations on the f-plane. An explanation of this oscillatory behavior late in the life cycle of the waves will be provided in a future publication.

Acknowledgments. We would like to thank Dr. Steven Karpik for many discussions on numerical methods. Khader Khan and Raul Cunha drafted some of the diagrams. All of the computation reported here were performed on the CRAY X-MP supercomputer of the Ontario Centre for Large Scale Computation located at the University of Toronto. Research support was from NSERC Grant A9627, an AES Science Subvention, and from a research grant from CRAY Research, Inc.

REFERENCES

Anderson, R. K., J. P. Ashman, F. Bittner, G. R. Farr, E. W. Ferguson, V. J. Oliver and A. H. Smith, 1977: Application of Meteorological Satellite Data in Analysis and Forecasting. ESSA. Tech. Rep. NESC 51.

Arakawa, A., 1966: Computational design for long term integration of the equations of motion: Two-dimensional incompressible flow. Part I. *J. Comput. Phys.*, **1**, 119–143.

Asselin, R., 1972: Frequency filter for time integrations. *Mon. Wea. Rev.*, **100**, 487–490.

Bjerknes, J., 1919: On the structure of moving cyclones. *Geofys. Publ. I.* (Reprinted in *Selected Papers of J. Bjerknes*), M. J. Wurtele, Ed., Western Periodicals, 606 pp.

——, and H. Solberg, 1923: Life cycle of cyclones and the polar front theory of atmospheric circulation. *Geofys. Publ. 3. Selected papers of J. Bjerknes*, M. J. Wurtele, Ed., Western Periodicals, 606 pp.

Boyle, J. S., and L. F. Bosart, 1983: A cyclone/anticyclone couplet over North America: An example of anticyclone evolution. *J. Atmos. Sci.*, **111**, 1025–1045.

——, and ——, 1986: Cyclone–anticyclone couplets over North America. Part II: Analysis of a major cyclone event over the eastern United States. *J. Atmos. Sci.*, **114**, 2432–2465.

Browning, K. A., and G. A. Monk, 1982: A simple model for the synoptic analysis of cold fronts. *Quart. J. Roy. Meteor. Soc.*, **108**, 435–452.

Carlson, T. N., 1980: Airflow through midlatitude cyclones and the comma cloud pattern. *Mon. Wea. Rev.*, **108**, 1498–1509.

Clark, T. L., 1977: A small-scale dynamic model using a terrain-following coordinate transformation. *J. Comput. Phys.*, **24**, 186–215.

——, 1979: Numerical simulations with a three-dimensional cloud model: Lateral boundary condition experiments with multicellular severe storm simulations. *J. Atmos. Sci.*, **36**, 2191–2215.

Eady, E. T., 1949: Long waves and cyclone waves. *Tellus*, **1**, 33–52.

Emanuel, K., 1986: Overview and definition of mesoscale meteorology. *Mesoscale Meteorology and Forecasting*, P. S. Ray, Ed., Amer. Meteor. Soc.

Gill, A. E., 1982: *Atmosphere-Ocean Dynamics.* Academic Press, 662 pp.

Golding, B., 1984: A study of the structure of mid-latitude depressions in a numerical model using trajectory techniques. I: Development of ideal baroclinic waves in dry and moist atmospheres. *Quart. J. Roy. Meteor. Soc.*, **110**, 847–879.

Haltiner, G. J., and R. T. Williams, 1980: *Numerical Prediction and Dynamic Meteorology.* Wiley and Sons, 477 pp.

Heckley, W. A., and B. J. Hoskins, 1982: Baroclinic waves and frontogenesis in a non-uniform potential vorticity semi-geostrophic model. *J. Atmos. Sci.*, **39**, 1999–2016.

Hoskins, B. J., 1976: Baroclinic waves and frontogenesis. Part I: Introduction and eady waves. *Quart. J. Roy. Meteor. Soc.*, **102**, 103–122.

——, 1983: Dynamical processes in the atmosphere and the use of models. *Quart. J. Roy. Meteor. Soc.*, **109**, 1–21.

——, and F. P. Bretherton, 1971: Atmospheric frontogenesis models: Some solutions. *Quart. J. Roy. Meteor. Soc.*, **97**, 139–153.

——, and F. P. Bretherton, 1972: Atmospheric frontogenesis models: Mathematical formulation and solutions. *J. Atmos. Sci.*, **29**, 11–37.

——, and N. V. West, 1979: Baroclinic waves and frontogenesis. Part II: Uniform potential vorticity jet flows—cold and warm fronts. *J. Atmos. Sci.*, **36**, 1663–1680.

——, and W. A. Heckley, 1981: Cold and warm fronts in baroclinic waves. *Quart. J. Roy. Meteor. Soc.*, **107**, 79–90.

Houze, R. A., and P. V. Hobbs, 1982: Organization and structure of precipitating cloud systems. *Adv. Geophys.*, **24**, 225–305.

James, I. N., and L. J. Gray, 1985: Concerning the effect of surface drag on the circulation of a baroclinic planetary atmosphere. *Quart. J. Roy. Meteor. Soc.*, **112**, 1231–1250.

Keyser, D., 1989: Numerical models of midlatitude cyclones: A mesoscale perspective. *IAMAP Conf.*, Reading, England.

——, B. D. Schmidt and D. G. Duffy, 1989: A technique for representing three-dimensional vertical circulations in baroclinic disturbances. *Mon. Wea. Rev.*, **117**, 2463–2494.

MacVean, M. K., 1985: Long wave growth by baroclinic processes. *J. Atmos. Sci.*, **42**, 325–334.

Moore, G. W. K., and W. R. Peltier, 1987: Cyclogenesis in frontal zones. *J. Atmos. Sci.*, **44**, 384–409.

——, and ——, 1990: Nonseparable baroclinic instability. Part II: Primitive equations dynamics. *J. Atmos. Sci.*, **47**, 1223–1241.

Mudrick, S. E., 1974: A numerical study of frontogenesis. *J. Atmos. Sci.*, **31**, 869–892.

Nakamura, N., and I. M. Held, 1989: Nonlinear equilibration of two-dimensional eady waves. *J. Atmos. Sci.*, **46**, 3055–3064.

Ogura, Y., and N. A. Phillips, 1962: Scale analysis of deep and shallow convection in the atmosphere. *J. Atmos. Sci.*, **19**, 173–179.

Palmèn, E., and C. W. Newton, 1969: *Atmospheric Circulation Systems.* Academic Press, 603 pp.

Peltier, W. R., and T. L. Clark, 1979: The evolution and stability of finite-amplitude mountain waves. Part II: Surface drag and severe downslope windstorms. *J. Atmos. Sci.*, **36**, 1498–1529.

——, J. Hallé and T. L. Clark, 1978: The evolution of finite amplitude kelvin helmholtz billows. *Geophys. Astrophys. Fluid Dyn.*, **10**, 53–87.

——, G. W. K. Moore and S. Polavarapu, 1988: Cyclogenesis and frontogenesis. Preprints, *Palmén Memorial Symp. on Extratropical Cyclones*, Helsinki, 83–89.

——, —— and ——, 1990: Cyclogenesis and frontogenesis. *Tellus*, **42A**, 3–13.

Polavarapu, S. M., 1989: Midlatitude cyclones and cyclogenesis. Ph.D. thesis, University of Toronto, 277 pp.

Randel, W. J., and J. L. Stanford, 1985: The observed Life Cycle of a baroclinic instability. *J. Atmos. Sci.*, **42**, 1364–1373.

Scorer, R., 1986: *Cloud Investigation by Satellite.* Ellis Horwood.

Shapiro, M. A., 1989: The mesoscale structure of extratropical marine cyclones. *Proc. of IAMAP*, Abstract Vol. 2, Reading, U.K.

——, and D. Keyser, 1990: Fronts, Jet Streams and the Tropopause. *Extratropical Cyclones.* Palmén Memorial Volume. C. W. Newton, E. Holopainen, Eds., Amer. Meteor. Soc. Chap. 10, in press.

Shuman, F. G., 1962: Numerical experiments with the primitive equations. *Proc. Int. Symp. on Numerical Weather Prediction*, Tokyo, Japan Meteor. Agency, 85–107.

Simmons, A. J., and B. J. Hoskins, 1978: The life cycles of some nonlinear baroclinic waves. *J. Atmos. Sci.*, **35**, 414–432.

——, and ——, 1980: Barotropic influences on the growth and decay of nonlinear baroclinic waves. *J. Atmos. Sci.*, **37**, 1679–1684.

Simons, T. J., 1972: The nonlinear dynamics of cyclone waves. *J. Atmos. Sci.*, **29**, 38–52.

Smolarkiewicz, P., 1983: A simple positive definite advection scheme with small implicit diffusion. *Mon. Wea. Rev.*, **111**, 479–486.

——, 1986: The multidimensional positive definite advection transport algorithm. Further development and applications. *J. Comput. Phys.*, **67**, 396–438.

Takayabu, I., 1987: Roles of the horizontal advection on the formation of surface fronts and on the occlusion of a cyclone developing in the baroclinic westerly jet. *J. Meteor. Soc. Japan*, **64**, 329–345.

Weldon, R., 1979: Cloud patterns and the upper air wind field. Air Weather Service Tech. Rep. 79,003.

Wood, R. A., 1988: Unstable waves on oceanic fronts: Large amplitude behavior and mean flow generation. *J. Phys. Oceanogr.*, **18**, 775–787.

Young, M. V., G. A. Monk and K. A. Browning, 1987: Interpretation of satellite imagery of A rapidly deepening cyclone. *Quart. J. Roy. Meteor. Soc.*, **113**, 1089–1115.